

Article

Carbon Nanotubes in Cement—A New Approach for Building Composites and Its Influence on Environmental Effect of Material

Teobald Kupka ^{1,*}, Natalina Makieieva ¹, Paweł Świsłowski ², Małgorzata Rajfur ², Artur Małolepszy ³, Leszek Stobiński ³, Stefania Grzeszczyk ⁴, Krystian Jurowski ⁴, Adam Sudoł ⁵, Roman Wrzałik ^{6,7}, Oimahmad Rahmonov ⁸ and Krzysztof Ejsmont ^{1,*}

- ¹ Faculty of Chemistry and Pharmacy, Opole University, 48, Oleska Street, 45-052 Opole, Poland; makieievium@gmail.com
 - ² Institute of Biology, University of Opole, 22, Oleska Street, 45-032 Opole, Poland; pawel.swislowski@uni.opole.pl (P.Ś.); rajfur@uni.opole.pl (M.R.)
 - ³ Faculty of Chemical and Process Engineering, Warsaw University of Technology, 1, Waryńskiego Street, 00-645 Warsaw, Poland; artur.malolepszy@pw.edu.pl (A.M.); lstob50@hotmail.com (L.S.)
 - ⁴ Faculty of Civil Engineering and Architecture, Opole University of Technology, 48, Katowicka Street, 45-061 Opole, Poland; s.grzeszczyk@po.edu.pl (S.G.); k.jurowski@po.edu.pl (K.J.)
 - ⁵ Department of Technical Sciences, University of Applied Sciences in Nysa, 5 Obrońców Tobruku, 48-300 Nysa, Poland; adam.sudol@pans.nysa.pl
 - ⁶ A. Chełkowski Institute of Physics, University of Silesia, 75 Pułku Piechoty 1, 41-500 Chorzów, Poland; rwrzalik@gmail.com
 - ⁷ Institute of Material Science, University of Silesia, 75 Pułku Piechoty 1a, 41-500 Chorzów, Poland
 - ⁸ Institute of Earth Sciences, Faculty of Natural Sciences, University of Silesia in Katowice, 60, Będzińska, 41-200 Sosnowiec, Poland; oimahmad.rahmonov@us.edu.pl
- * Correspondence: teobaldk@gmail.com (T.K.); ejsmont@uni.opole.pl (K.E.)



Citation: Kupka, T.; Makieieva, N.; Świsłowski, P.; Rajfur, M.; Małolepszy, A.; Stobiński, L.; Grzeszczyk, S.; Jurowski, K.; Sudoł, A.; Wrzałik, R.; et al. Carbon Nanotubes in Cement—A New Approach for Building Composites and Its Influence on Environmental Effect of Material. *Molecules* **2024**, *29*, 5379. <https://doi.org/10.3390/molecules29225379>

Academic Editor: Shaojun Yuan

Received: 28 October 2024

Revised: 8 November 2024

Accepted: 13 November 2024

Published: 14 November 2024



Copyright: © 2024 by the authors. Licensee MDPI, Basel, Switzerland. This article is an open access article distributed under the terms and conditions of the Creative Commons Attribution (CC BY) license (<https://creativecommons.org/licenses/by/4.0/>).

Abstract: An addition of carbon nanostructures to cement paste is problematic due to the difficulties in obtaining homogenous mixtures. The paper reports on a more effective way of mixing carboxylated multi-walled carbon nanotubes (MWCNT-COOH) in cement pastes. The additional biological impact of the studied nanomodified cement was analyzed in the case of two moss species' vitality. The applied approach of obtaining a homogeneous mixture is based on intense mechanochemical mixing of MWCNT-COOH together with polycarboxylate superplasticizer (SP). As a result, a more homogenous suspension of MWCNT-COOH within a liquid superplasticizer, suitable for addition to hydrophilic cement paste, was obtained. FT-IR/Raman spectroscopy was used for materials' characterization. To explain the mixing process at the molecular level, systematic theoretical studies using density functional theory (DFT) were performed. The structures, interaction energies and IR/Raman vibrational spectra of model carboxylic acids, mixed with functionalized SWCNTs as simplified models of real MWCNTs, were obtained. Due to the controversial opinions on the environmental hazards of carbon nanostructures, additional in vivo studies were performed. In this case, effects of cement modified by the addition of small amounts of MWCNT-COOH with SP in comparison to the composite without carbon nanostructures and control subsoil on the vitality of mosses *Polytrichum formosum* and *Pseudoscleropodium purum* were studied.

Keywords: multi-walled carbon nanotubes; superplasticizer; homogenization; FT-IR; Raman; DFT; intermolecular interaction; mosses; vitality

1. Introduction

Properties of current composites based on cement are improved by the addition of small amounts of various nanoparticles. However, the effect of these additives on the physico-chemical properties of the high-performance final product is critically dependent

on the applied particles' and nanoadmixture's homogeneous distribution within the mix, e.g., without their agglomeration [1].

There are several methods leading to homogeneous nanoparticle distribution without agglomeration. For example, the parallel use of efficient superplasticizers, sonification and fast mixing in cement mortar was reported [2]. However, mechanical mixing applied for degradation of the formed agglomerates of nanoparticles is not efficient [3]. The introduction of nanoparticles to concrete mix in the form of water suspension with the application of sonification is also an efficient way [4]. A detailed analysis of the effect of MWCNT nanoparticles' addition on mechanical properties of cement matrix was reported [5]. For this reason, the design of new mixing methods is an important question in the production of material with better qualities. From the above studies, it is apparent that the addition of surfactants, which decrease surface tension and additionally show hydrophilic properties, supporting dispersion of partly hydrophobic MWCNT particles, is essential for cement paste.

It is known that the introduction of carbon nanotubes and other ordered carbon materials into the cement mix and the preparation of homogeneous mixture are difficult due to their agglomeration as well as transposition and annihilation between some clusters and/or cells, strain–stress and inner surface topography. This process is partly controlled by the formation of hydrogen bonds and, to some extent, the van der Waals interactions between the functionalized nanocarbon particles [6] and therefore an efficient dispersion of carbon nanoparticles in cement composites is necessary. This is achieved by using sonification and applying surfactants, for example, sodium dodecyl benzene sulfonate [7], sodium dodecyl sulfate [8], or an acid treatment [9], leading to functionalization of nanocarbon structures with polar groups containing oxygen (including -OH and -COOH) [10].

There have been many studies on the formation of a covalent bond between MWCNTs and various substituents, which provides changes in material hydrophilicity [9,11]. For example, groups like -OH, -COOH, -NH₂ and grafted long acryl chains were permanently introduced to make carbon nanomaterials more hydrophilic, thus improving their mixing and dispersion in water [12]. In our earlier reports [13,14] we analyzed theoretically the structure and properties of functionalized single-walled carbon nanotubes (SWCNTs). On the other hand, experimental nanocarbon characterization using vibrational spectroscopy, including infrared (IR) and Raman techniques, is widely used [15,16]. There are several basic works on the IR technique, as well as on its application for characterization of organic systems including polymers [17–23]. Raman spectroscopy of single- and multi-walled carbon nanotubes, graphite and graphene, including graphene oxide (GO) and reduced graphene oxide (rGO), is also well documented [24–34]. Due to the polymeric nature of the used superplasticizers, their structure can be analyzed using IR and Raman techniques. Contrary to Raman studies, the presence of water nearly completely excludes IR measurements. On the other hand, a versatile nuclear magnetic resonance (NMR) technique is suitable for the study of polymers in water.

In the current study, we use a molecular modeling approach in order to obtain a deeper insight into the role of small nanocarbon additions, including functionalized MWCNTs, leading to the production of a homogenous nanocarbon suspension with superplasticizer. This could finally lead to obtaining cement materials with improved properties. The most important stage of the addition of carbon-containing (and other materials) nanofiller to cement paste is related to homogenous suspension preparation of functionalized MWCNTs or graphene in water. This is due to the fact that side walls of carboxylated nanotubes are mainly hydrophobic and their ends are functionalized with polar -COOH and -OH groups [15,16]. It is also known [15,16] that the amount of sidewall functionalization is much smaller than at their terminals. Thus, we concentrated on preparation of a nanocarbon suspension in superplasticizer for subsequent mixing with cement. In fact, the superplasticizer acts as a kind of surfactant for carbon nanotubes [35].

It is known that hydrophobic interactions promote agglomeration of several nanotubes and decrease their ability to mix with water. Additionally, as a result of strong hydrogen

bonding, their ends could also stick together and hinder mixing with water [36]. However, the addition of polymeric superplasticizer with several polar groups could lead to direct H bond interactions with nanotube “hydrophilic hot spots”. Thus, the presence of superplasticizer in the liquid phase enables formation of strong interactions between MWCNT-COOH and long polymer chains, which additionally could wrap around the carbon nanotubes and thus improve their mixing with water. This process is schematically shown in Figure 1. A similar wrapping of long chains of polysaccharide (amylose) around carbon nanotubes was observed earlier [36,37]. The beneficial role of polymeric surfactants with long hydrophobic chains and polar heads in improving dispersion of carbon nanotubes was reported [35]. In a schematic cartoon, the authors [35] nicely explained the surfactant action by utilizing non-covalent dispersion interactions between non-polar surfactant chains with the hydrophobic side of carbon nanotubes. We want to admit that in the current work we do not study markedly weaker dispersion forces or interactions with -OH groups because we postulate a significantly stronger interaction between hydrophilic -COOH and COO-groups of the superplasticizer and “sensitive spots” of functionalized nanotubes. These non-covalent interactions should result in better dispersion of carbon nanomaterials in water (see Figure 1).

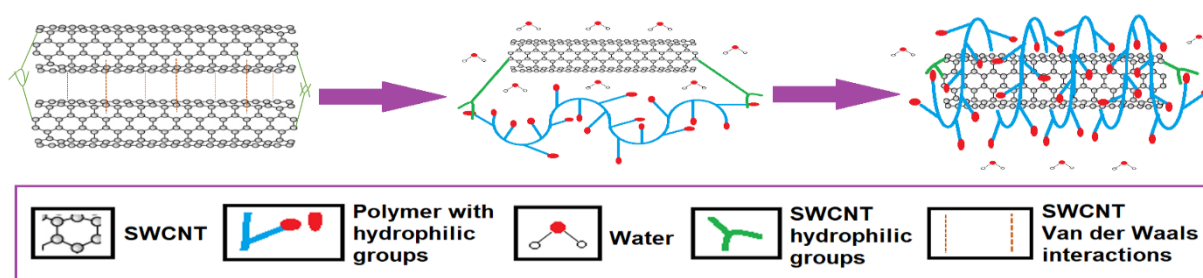


Figure 1. Schematic diagram explaining the interaction between polar groups of superplasticizer and carbon nanotubes, partly covered with carboxylic (and some hydroxyl) groups. Left, middle and right schemes show three stages of interaction between superplasticizer and carbon nanotube.

In the current study, commercial polycarboxylate superplasticizer and MWCNT-COOH [38,39] were characterized by Fourier transform infrared (FT-IR) and Raman spectroscopy. To explain the mixing process mentioned above at the molecular level, we decided to use theoretical modeling within a framework of density functional theory (DFT [40–42]). Another important aspect of the introduction of carbon nanostructures into building materials is environmental safety of the final composite. There are controversial opinions on nanomaterials’ effect on the vitality of different living organisms. Some studies demonstrate a negative influence of high concentrations of nanomaterials, but negligible changes are observed for smaller amounts of graphene-based materials [43,44]. For this reason, a biological study was carried out, analyzing the effect of pure cement paste and a paste modified by the addition of MWCNT-SP on the photosynthetic activity of living organisms, e.g., two species of mosses. These plants, as pioneer organisms, could be used to colonize anthropogenic areas and combat the so-called “concretomania”.

Mosses (Bryophyta) are small eukaryotic non-vascular plants, which usually have no internal transport system. They have a flowerless life cycle and form rhizoids as a primitive analogue of a “true” root system. As pioneer organisms, mosses occupy urbanized areas, as well as places where higher plants cannot survive due to high temperature (desert), altitude or limited light (tundra) [45]. High resistance to stressful living conditions makes mosses good candidates for biomonitoring of environmental pollution. The main advantages of using these organisms as bioindicators are a lack of crust, i.e., moss tissues are readily permeable to micro- and macronutrients, high cation exchange capacity and easy plant material availability (their colonies grow relatively fast). Other advantages of studies with moss research material are their low cost and short duration of experiments [46]. However, there are some complications with biomonitoring using mosses. Colonization of these

organisms is dependent on various factors such as humidity [47]. An example is green roofs, where the depth of the substrate and the age of the roof have a dominant influence on the structure of the plant communities on it. Thin substrates and young roofs support sedum and moss species [48]. The moss layer transfer technique significantly increases the presence of moss species that were introduced during restoration. The presence of forest bryophyte species in spreading material increases their biomass in the restoration site, even on a thick residual *Sphagnum* peat layer [49]. Another use for mosses in urban areas is urban greening. They absorb and retain water, reducing surface water run-off, thus protecting the area from flooding and drying [50,51]. Due to the high availability of mosses in the urban environment they could be good model organisms for studying nanomodified materials' harmful effects. For this reason, it seems to be useful to investigate the effects of MWCNT-modified cement paste on the viability of the mosses *Polytrichum formosum* Hedw. and *Pseudoscleropodium purum* (Limpr) M. Fleisch. ex Broth. These species are often found in European forests and could be transplanted, for example, into urban spaces.

2. Results and Discussion

FT-IR studies of carbon nanotubes and graphenes are extremely challenging due to the presence of tightly bound water and the obtained spectra are noisy, broad and nearly featureless. For brevity, an example of FT-IR spectra of MWCNTs is shown in Figure S1 in the Supplementary Materials.

2.1. Superplasticizer Characterization by FT-IR Spectroscopy

In the first step, the applied superplasticizer was characterized using ATR and infrared spectroscopy (see Figures 2 and 3). On the other hand, the ATR spectrum (see Figure 2), which does not need sample preparation before measurement, included the main spectral features preserved though some peaks were overlapped and shifted by a few wavenumbers. The observed peaks of the superplasticizer from Figure 3 were tentatively assigned and are gathered in Table 1.

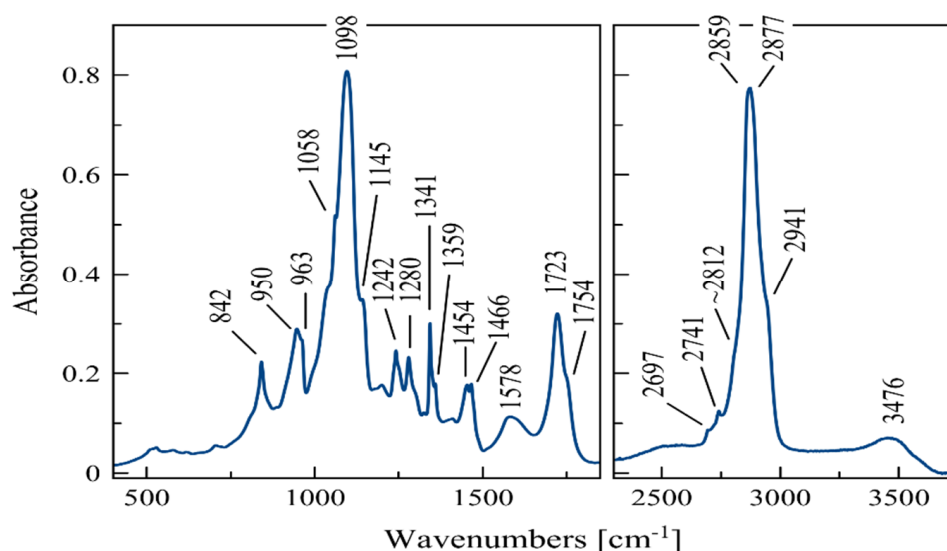


Figure 2. Selected fragments of the ATR spectrum of superplasticizer (SP) with peaks labeled. Partly overlapped peaks are clearly visible.

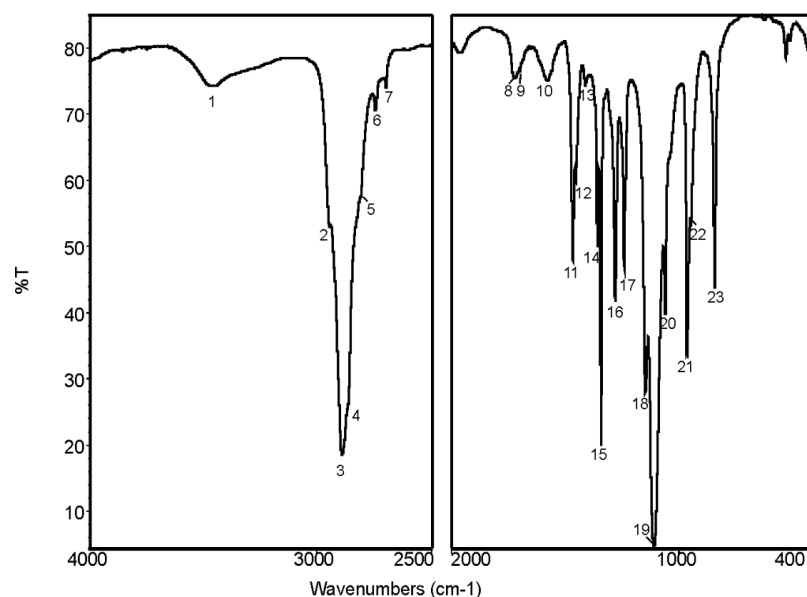


Figure 3. Selected fragments of the FT-IR spectrum of superplasticizer with peaks labeled.

Table 1. Position (in cm^{-1}) and tentative assignment of the FT-IR absorption bands ^a of the superplasticizer.

Peak	Wavenumber	Assignment	Structural Fragment
1	3462	OH str	-OH hydroxyl group
2	2944	$\text{CH}_2(\text{O})$ asym str	$-\text{CH}_2(\text{O})$ methylene group adjacent to oxygen
3	2888	$\text{CH}_2(\text{O})$ sym str	$-\text{CH}_2(\text{O})$ methylene group adjacent to oxygen
4	~2862	CH_2 str	$-\text{CH}_2-$ methylene group in polymer chain
5	~2806	CH str	Methine group in polymer chain (near $\text{C}=\text{O}$)
6	2741	$2 \times \text{CH}_2$ sciss	Overtone of the 1360cm^{-1} band
7	2692	$2 \times \text{CH}_2$ sciss	Overtone of the 1343cm^{-1} band
8	1728	$\text{C}=\text{O}$ str	$\text{O}=\text{C}-\text{OR}$ ester
9	1705	$\text{C}=\text{O}$ str	$\text{O}=\text{C}-\text{OH}$ carboxyl (acid)
10	1578	COO^- asym str	$-\text{COO}^-$ carboxylate (salt)
11, 12	1467, 1455	CH_2, CH def	CH_2 and CH aliphatic methylene and methine
13	1412	COO^- sym str	$-\text{COO}^-$ carboxylate (salt)
14, 15	1360, 1343	CH_2 sciss	$-\text{CH}_2-$ methylene group in ethylene fragment
16, 17	1280, 1242	$\text{CCO} + \text{C}-\text{O}-\text{C}$ str	$\text{O}=\text{C}-\text{OR}$ ester
18, 19	1149, 1110	$\text{C}-\text{O}-\text{C}$ asym str	$\text{H}_2\text{C}-\text{O}-\text{CH}_2-$ ether
20	1061	$\text{C}-\text{O}$ (H/C) str	$\text{C}-\text{O}(\text{H}) \text{C}-\text{O}(\text{C})$ bond in alcohols and esters
21, 22	964, 948	CH_2 rock	$-\text{CH}_2\text{CH}_2-$ ethylene fragment
23	843	CCO bend	$-\text{CH}_2\text{CH}_2-\text{O}-$ oxyethylene fragment

^a Mode abbreviations: str (stretch), bend (bending), def (deformation), sciss (scissoring) (in-plane bending), sym (symmetric), asym (asymmetric), rock (rocking).

The carbonyl stretching fragment ($1800\text{--}1500\text{ cm}^{-1}$) of the FT-IR spectrum with partly overlapped peaks, shown in Figure 3, was carefully analyzed and the individual peaks were labeled. In order to assign more precisely the type of functional groups containing a carbonyl fragment on the superplasticizer FT-IR spectrum, a digital line fitting procedure (deconvolution) was applied. As a result, the positions of partly overlapped signals

were determined. Examples of original spectral fragments and the resolved individual bands of neat superplasticizer alone and in the presence of 3% MWCNT suspension are shown in Figure 4A (left) and Figure 4B (right), respectively. As result, it was possible to observe quantitatively the presence of carboxylic acids ($-\text{COOH}$ at 1705 cm^{-1}), esters ($-\text{COOR}$ at 1728 cm^{-1}) and ionic salts ($-\text{COO}^- \text{ Me}^+$ at 1575 cm^{-1}) as fragments of SP molecules (Figure 4A (left)). In addition, it was apparent from Figure 4A that the strong band at 1635 cm^{-1} was due to the HOH bending mode of water. This band is missing in Figure 4B. In principle, it could originate from moisture present in KBr while the band at about 1660 cm^{-1} could originate from unsaturated and conjugated $\text{C}=\text{C}$ groups, possibly from MWCNTs.

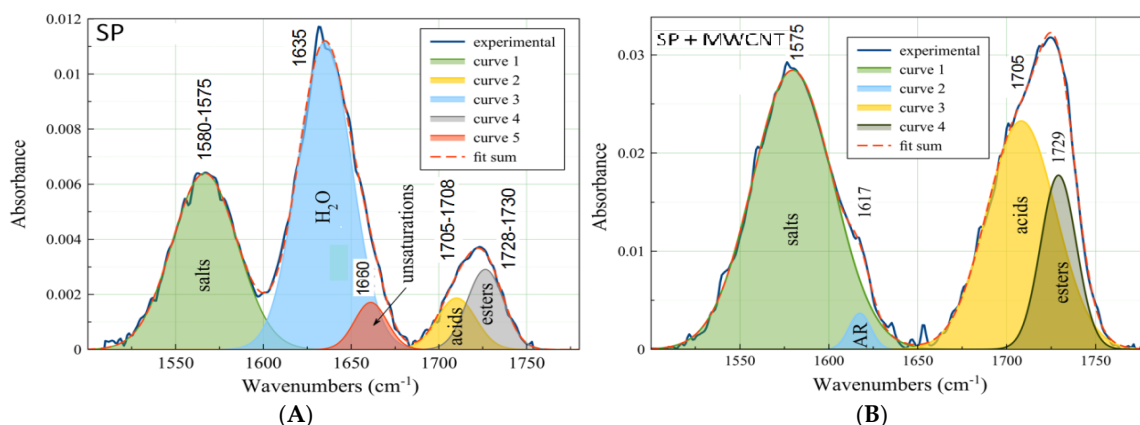


Figure 4. Carbonyl region fragment of FT-IR spectrum of (A) neat SP and (B) SP containing 3% MWCNT and the result of line fitting is also shown.

A simplified chemical structure of superplasticizer, as deduced from the analyzed IR spectra (compare Figures 2 and 4 and Table 1), indicates the presence of three main molecular fragments (building blocks):

- (1) Acids ($\text{R}-\text{COOH}$),
- (2) Salts ($\text{R}-\text{COO}^-$),
- (3) Esters ($\text{R}-\text{COOR}'$).

The surfactant properties of SP are due to its specific chemical structure formed by the building blocks. Thus, the superplasticizer molecule is formed by long backbone chains containing aliphatic methylene ($-\text{CH}_2-$) and methine ($-\text{CH}-$) groups, e.g., $-\text{CH}_2-\text{CH}-\text{CH}_2-\text{CH}-$ fragments, and long side oxyethylene chains ($-\text{CH}_2-\text{CH}_2-\text{O}-$)_n. Thus, it resembles a comb polymer structure, analyzed theoretically in solid polymer electrolytes with hopping lithium cation [52]. The main backbone chain of SP is non-polar while the side chains are highly hydrophilic, in particular due to their carboxylic terminal groups. Therefore, the applied SP shows the desired surfactant properties.

A detailed analysis of the measured infrared spectra of the applied superplasticizer (see results in Figures 3 and 4 and Table 1) allows the conclusion that its molecules contain methylene groups (CH_2) belonging to the backbone chain which are visible at about 2862 cm^{-1} . These moieties are formed by saturated polyacrylic fragments ($-\text{CH}_2-\text{CH}-\text{CH}_2-\text{CH}-$)_n and $-\text{CH}_2-$ units, directly bonded to oxygen atoms ($-\text{CH}_2-\text{O}-$) in side polyoxyethylene chains (see CH stretch vibrations at about 2944 and 2888 cm^{-1}). In fact, the strongest band in the IR spectrum of SP at 1110 cm^{-1} belongs to polyetheric fragments $-\text{CH}_2-\text{O}-\text{CH}_2-$. Its high intensity suggests the presence of a very long polyetheric ($-\text{CH}_2-\text{CH}_2-\text{O}-$) chain, containing dozens of units. By comparing the intensity of this C-O-C stretch vibration with earlier reports [53,54], one could assume the presence of over 80 units forming the side chain. Obviously, the non-polar, hydrophobic backbones of the superplasticizer polymer will have an affinity for the non-polar, hydrophobic surfaces of carbon nanoparticles. On the other hand, polar and strongly hydrophilic carboxylate groups of the sodium acrylate

ionic salt $\text{-COO}^- \text{Na}^+$ and long hydrophilic poly(oxyethylene) chains will show affinity to the water environment of the cement mix.

The structure elements discussed above and overall properties of superplasticizer could lead to better dispersion of carbon nanoparticles in the aqueous environment of cement mix.

2.2. Raman Spectroscopy of Neat Superplasticizer and with Added MWCNTs

The Raman spectra of neat superplasticizer, as well as with very small admixtures of MWCNTs, are shown in Figure 5 and the tentative signal assignment is presented in Table 1.

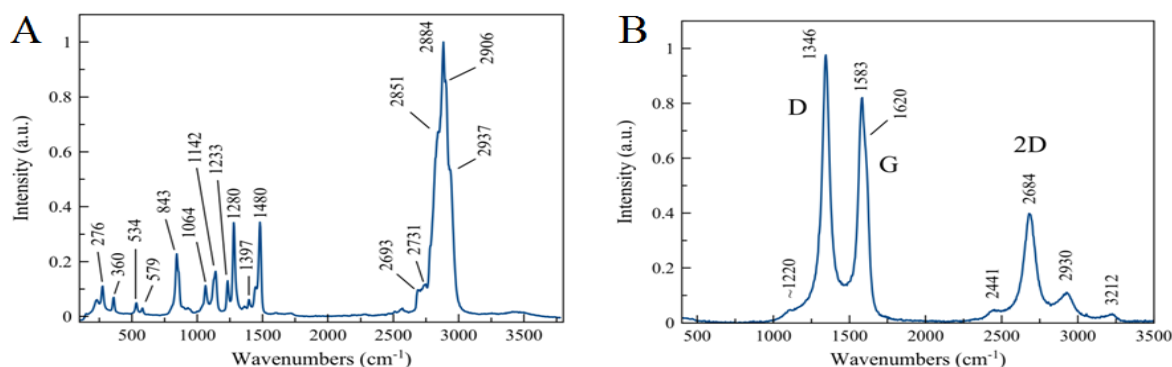


Figure 5. The Raman spectra of (A) neat superplasticizer and (B) SP + 3% MWCNTs.

Raman spectra of the original superplasticizer (sample A) and with the addition of 3% MWCNTs (sample B) are shown in Figure 5. It is also worth mentioning a significant increase in the viscosity and fluorescence of superplasticizer containing very small amounts of carbon nanomaterial. Thus, it was challenging to analyze such Raman spectra and was necessary to apply baseline correction and line fitting procedures first.

The IR and Raman data shown above provide complementary information. In particular, no MWCNTs are visible from IR data in samples containing small amounts of nanostructured carbon added to superplasticizer. However, Raman spectra in Figure 5 (sample B) clearly show characteristic D and G bands of nanostructured carbon materials at about 1346 and 1580 cm^{-1} . A similar ratio of D/G Raman bands was recently reported in cement paste containing a small amount of MWCNTs [55]. From the magnitude of the D band ($D > G$) we can conclude about the presence of significant structural disorder in the applied MWCNTs. In addition, in the range of 2440 to 3200 cm^{-1} several overtones and combination bands are observed due to the presence of carbon nanomaterial. In addition, Raman spectra of neat SP (sample A in Figure 5) reveal large signals due to CH and CH_2 stretch modes in the range of 2850 to 2940 cm^{-1} . This could be due to a repeated motif of methylene groups in oxoethyl- chains of superplasticizer, forming a kind of comb polymer.

In Table 2 the observed bands of superplasticizer (sample A) and SP in the presence of 3% MWCNTs (sample B) are gathered and the tentative peak assignments given. The apparent lack of superplasticizer, as observed from Raman spectra of sample B, seems to be confusing (see Table 2). On the other hand, very small amounts of carbon nanotubes (only 3% MWCNTs) are clearly visible (see characteristic D, G bands and their overtones and combination bands). However, very similar spectra of carbon materials in polymers were reported in the literature [56–58].

Table 2. Vibrational bands ^a (in cm⁻¹) in the Raman spectra of neat superplasticizer (sample A) and with addition of 3% MWCNTs (sample B).

No	A		B		Assignment
	Position	Intensity	Position	Intensity	
1			3212	vw	2G
2			2990	m	D + G
3	2937	sh			CH ₂ (O) asym str
4	2906	sh			
5	2884	vs			CH ₂ (O) sym str
6	2851	sh			CH ₂ str
7	2731	w			
8	2693	w			2 × CH ₂ sciss
9			2684	s	G' (2D)
10			~2441	vw	G*
11			1620	sh	G2
12			1583	vs	G (Tangential)
13	1480	m			CH ₂ , CH def
14	1397	vw			
15			1346	vs	D (Disorder)
16	1280	m			CCO + C-O-C str
17	1233	vw			CCO + C-O-C str
18			~1220	vw	
19	1142	m			C-O-C asym str
20	1064	w			C-O(H/C) str
21	843	m			CCO bend
22	579	vw			
23	534	vw			
24	360	vw			
25	276	w			

^a Mode abbreviations: str (stretch); bend (bending); def (deformation), sciss (scissoring) (in-plane bending); sym (symmetric), asym (asymmetric); m (middle); w (weak); vs (very strong); vw (very weak) and sh (shoulder).

2.3. Theoretical Modeling of Superplasticizer Interaction with Carbon Nanotubes

In order to model structural fragments of superplasticizer, carbon nanotubes and their mutual interactions, we decided to select two density functionals, BLYP and B3LYP, and check their performance on several small molecules.

2.3.1. Performance of BLYP, B3LYPD3BJ and BLYPD3BJ Density Functionals in Predicting Structure, Interaction Energy and Vibrational Parameters of Water Monomer and Dimer

Due to its small size, the water monomer is a convenient model for verifying the performance of lower-level theoretical methods, including DFT, with respect to benchmark CCSD(T) calculations [59]. The latter method is too expensive and will be used here only for comparison. In addition, the current theoretical results on water monomer could be directly compared with experiments in the gas phase [60], as well as with high-level theoretical calculations at the coupled cluster level of theory [61]. It is known that BLYP and B3LYP density functionals are able to model geometry and energy of hydrogen bonds, which are dominated by electrostatic interactions. However, to account for long-range dispersion

forces, also present as small components of H bonds, the use of empirical terms modeling these interactions, for example, the GD3BJ term, introduced by Grimme, is recommended. In our studies, we were interested in recovering the total electrostatic and dispersion effects and we applied the B3LYPD3BJ and BLYPD3BJ functionals. In addition, small carboxylic acids were selected as models of superplasticizer structure fragments. The possibility of carboxylic groups interacting with sodium and calcium cations and with functionalized carbon nanotubes was also taken into account.

For brevity, in Table S1 in the Supplementary Materials, geometrical and vibrational parameters of water monomer are compared, predicted by BLYP, B3LYPD3BJ and BLYPD3BJ density functionals, combined with a large and flexible aug-cc-pVTZ basis set against experiment and benchmark CCSD(T) results [60,61]. It is apparent that the selected density functionals predict very accurate OH bond length and HOH angle of the water monomer which deviate from experiments by 0.050–0.015 Å and 0.04–0.6°, respectively. Additionally, the structure of water, predicted without and with the D3BJ dispersion term, is the same. As expected, the benchmark coupled cluster method, combined with a large basis set [61], reproduces the experiment very well.

It is known [62–65] that in routine molecular modeling calculations, the predicted harmonic frequencies are not computationally expensive but, due to omission of anharmonicity, they significantly overestimate experiment. However, it is apparent from Table S1 that the water monomer wavenumbers of symmetric and asymmetric OH stretch and HOH deformation modes are very accurately predicted in both high-level harmonic and anharmonic CCSD(T) calculations (RMS < 3 cm⁻¹). On the other hand, B3LYPD3BJ/aVTZ calculations also produce acceptable and fairly accurate wavenumbers (RMS < 35 cm⁻¹). The corresponding BLYPD3BJ/aVTZ results are about five times worse. However, when the latter results are “treated” as fundamental ones, they reproduce experimental results extremely well (RMS ~1 cm⁻¹).

Prediction of water dimer geometry and interaction energy allows both the determination of forces, which keep two H bonded monomers together, and its molecular structure. However, with limited size basis sets, one has to take care about the basis set superposition error (BSSE [66]), for example, by applying the counterpoise method (CP [67]).

The results of unconstrained optimization of linear water dimer, which is the most stable one [68–74], using BLYPD3BJ and B3LYPD3BJ density functionals, combined with the aug-cc-pVTZ basis set, are included in Figure S2. It is apparent that the geometrical parameters calculated with both density functionals are very similar but the counterpoise-corrected interaction energies, calculated with the former method, are significantly closer to the benchmark CCSD(T) result (−4.94 vs. −5.02 kcal/mol [68], see Table S2). Very accurate BLYPD3BJ interaction energies of H bonded dimers (close to CCSD(T) results) in comparison to B3LYPD3BJ were also reported by Řezáč [75].

Apart from interaction energy, in Table S2 are also gathered structural and vibrational parameters of water dimer, calculated with BLYPD3BJ and B3LYPD3BJ density functionals and using the aug-cc-pVTZ basis set and compared with the available experimental and benchmark coupled cluster results [65,68,69,76–80]. Obviously, the distances calculated with BLYPD3BJ are somewhat longer than the corresponding B3LYPD3BJ ones but still very accurate. It is also evident from Table S2 that both CCSD(T) and DFT methods predict vibrational frequencies with lower accuracy than structural parameters. However, the B3LYPD3BJ predicts water dimer wavenumbers about three times better than BLYPD3BJ. Additionally, one has to remember that to obtain better agreement with the observed IR/Raman data, the theoretical vibrations are often scaled [81].

2.3.2. Monomer and Dimer Properties of Formic and Acetic Acids

The next two briefly tested model molecules are formic and acetic acids. These compounds have been studied using both experimental and theoretical methods [82–108]. The BLYPD3BJ and BLYP optimized structures of *trans* conformers of carboxylic acids, which are the most stable ones, are shown in Figure S3. It is apparent from Table S3 that

both BLYPD3BJ- and BLYP-calculated formic and acetic acid bond lengths very accurately reproduce experiment and benchmark theoretical results (RMS deviations of 0.008–0.022 Å, see [83,85,86,89–91,105]). In particular, the B3LYP results closely reproduce CCSD(T) data. However, as expected, these results are somewhat worse than those obtained from very expensive computations at both CCSD and CCSD(T) levels of theory [86,109].

The selected level of DFT theory (BLYP/aVTZ and BLYPD3BJ/aVTZ) is also able to predict fairly accurate harmonic vibrations of formic acid monomer [86,89,91,105,110] and the RMS deviations of about 31 cm^{-1} with respect to experimental IR and Raman data, as well as benchmark coupled cluster results, are relatively small (see Table S4). However, the corresponding VPT2-calculated RMS of about 96 cm^{-1} is very bad. Interestingly, the harmonic vs. anharmonic values for B3LYP (and B3LYPD3BJ) show the opposite trend (Table S4C, RMS of 68 and 22 cm^{-1}). It is apparent from Table S4 that the harmonic BLYP frequencies are over two times better than the B3LYP ones.

However, the accuracy of theoretical interatomic distances and vibrational frequencies of formic acid monomer is lower than in the case of water monomer (see Tables S3 and S4). On the other hand, the anharmonic (VPT2) frequencies calculated by BLYP and BLYPD3BJ density functionals are unacceptable (RMS of $\sim 100\text{ cm}^{-1}$, see Table S4B).

The BLYP-optimized structure of a typical formic acid dimer, formed by two neutral formic acid molecules, together with indicated bond lengths without and with inclusion of dispersion, is shown in Figure 6A. The cyclic dimer is held by two BLYP- and BLYPD3BJ-estimated H bonds differing by only $\sim 0.03\text{ Å}$.

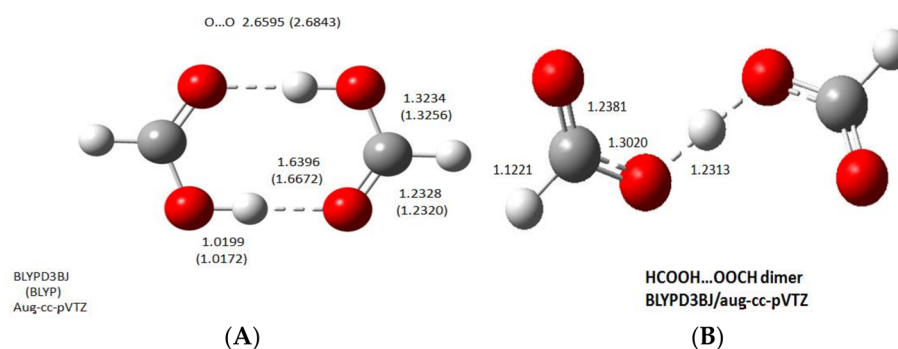


Figure 6. BLYPD3BJ- and BLYP-optimized structures of (A) *trans*-formic acid dimers and “mixed dimer HCOOH...OOCH” (B) (interatomic distances are in Å).

The other “mixed” formic acid dimer is formed by its anion and a neutral molecule (Figure 6B). The BLYPD3BJ- and B3LYPD3BJ-calculated interatomic distances are also shown in the scheme. Very short H bonds indicate strong interactions.

As before, both BLYPD3BJ and BLYP density functionals predict similar (but not identical) formic acid dimer interatomic distances (see Figure 6A and Table S6) and very accurately reproduce coupled cluster [86] and experimental results [90,105] (deviation of 0.01–0.03 Å). However, there is a significant difference in the optimized structure shown in Figure S2B, predicted by BLYP and BLYPD3BJ density functionals. In other words, upon inclusion of dispersion effects, the H atom is more localized at one formate molecule and the other shows a more pronounced carboxylic anion structure. Thus, the former functional predicts the carboxylic H atom exactly in the middle between two oxygen atoms (H...O of 1.2313 Å) and the O...O separation is 2.4574 Å. The latter density functional produces an asymmetric H bond with the H atom localized closer to one oxygen atom (O...H distances are 1.1734 and 1.2974 Å). Additionally, the O...O distance is slightly shorter (2.4654 Å).

There are 24 normal modes of formic acid dimer [86,94–96,110]. Both density functionals predict its vibrational frequencies reasonably well with RMS deviations from 20 to 40 cm^{-1} (Tables S7 and S8). However, the inclusion of an empirical dispersion term slightly deteriorates the accuracy of the predicted vibrations.

A very similar structure to formic acid dimer was obtained for acetic acid dimer (Figure S4), too. The corresponding harmonic and anharmonic frequencies for acetic acid dimer, calculated with BLYP and B3LYP density functionals (with and without the GD3BJ term), are gathered in Table S9. In this case, B3LYP predicts some anharmonic vibrations higher than the corresponding harmonic ones.

It is known that both formic and acetic acids form very strong dimers which are also present in the gas phase [93]. Thus, it was interesting to calculate the corresponding interaction energies holding two monomers in a dimer (see Table 3).

Table 3. Raw and CP-corrected interaction energy (in kcal/mol) of formic and acetic acid dimers. The magnitude of dispersion and BSSE are also evaluated.

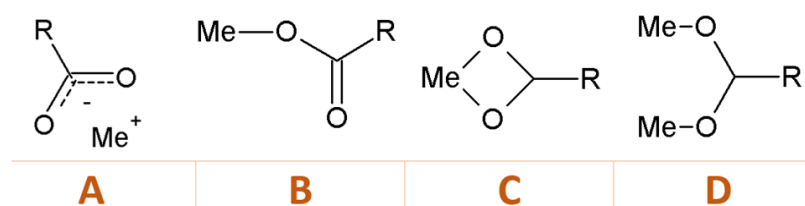
Method	Interaction Energy	Dispersion	% Dispersion	BSSE
Formic acid dimer				
Optimized and SP calculated with 6-31+G*				
BLYP (raw)	−17.23			1.19
BLYP (CP)	−16.04			
Optimized with 6-31+G*, SP calculated with aug-cc-pVTZ				
BLYP (raw)	−17.41			0.23
BLYP (CP)	−17.18			
Optimized with 6-31+G*, SP calculated with aug-cc-pV5Z				
BLYP (raw)	−17.34			0.02
BLYP (CP)	−17.32			
Optimized and SP calculated with aug-cc-pVTZ				
BLYP (raw)	−17.53			0.25
BLYP (CP)	−17.28			
BLYPD3BJ (raw)	−20.89	−3.36	16.08	0.26
BLYPD3BJ (CP)	−20.63	−3.35	16.24	
B3LYP (raw)	−18.42			0.26
B3LYP (CP)	−18.16			
B3LYPD3BJ (raw)	−21.15		12.91	0.26
B3LYPD3BJ (CP)	−20.89	−2.73	13.07	
CCSD(T)/aTZ ^a	−19.7			
CCSD(T)/CBS ^b	−18.61			
Acetic acid dimer				
Optimized and SP calculated with aug-cc-pVTZ				
BLYP (raw)	−18.36			0.29
BLYP (CP)	−18.07			
BLYPD3BJ (raw)	−22.00	−3.64	16.55	0.30
BLYPD3BJ (CP)	−21.70	−3.63	16.73	
B3LYP (raw)	−19.20			0.29
B3LYP (CP)	−18.91			
B3LYPD3BJ (raw)	−22.16		13.36	0.29
B3LYPD3BJ (CP)	−21.87	−2.96	13.53	
CCSD(T)/aTZ ^a	−20.8			
Lit. ^b	−14.16			

^a Single-point CCSD(T) on MP2/aug-cc-pVTZ geometry, from ref. [104]; ^b CCSD(T)/CBS(aTZ,aQZ) result, from ref. [111].

The benchmark interaction energy for *trans*-formic acid dimer calculated at the CCSD(T)/CBS level of theory is -18.753 kcal/mol [94,112,113]. From the energy difference between BLYP and BLYPD3BJ results, it was possible to see a significant contribution of dispersion in the total interaction energy (14 and 20% for formic and acetic acid dimers). It was observed that the accuracy of structure optimization has a small effect on the value of the interaction energies. Higher-level theory interaction energies, such as aug-cc-pVTZ and aug-cc-pV5Z, differ only a little. It is worth noticing that our BLYP result for formic acid dimer is close to benchmark coupled cluster results. Interestingly, for the applied aug-cc-pVTZ basis set, a fairly small BSSE was calculated (about 0.25–0.30 kcal/mol). Single-point CCSD(T) calculation with a very large basis set (aug-cc-pV5Z) indicated a very small basis set superposition error (0.02 kcal/mol).

2.3.3. Performance of BLYP, B3LYPD3BJ and BLYPD3BJ Density Functionals in Predicting Structure, Interaction Energies and Vibrational Frequencies of Formic and Acetic Acid Salts with Na^+ and Ca^{2+}

Molecules of superplasticizer could strongly interact with polar groups of carbon nanotubes forming typical carboxylic dimers $\text{R-COOH} \dots \text{HOOC-R}'$ or partly ionized $\text{R-COOH} \dots (\text{OOC-R})^-$ ones. Obviously, the presence of metal cation Me^+ will lead to differently charged structures like $\text{R-COO-Me}^+-\text{OOC-R}$. The structure patterns of metal carboxylates depend on the type of cation [114] and the dominating structures for sodium and calcium are structures A and C, respectively (see Scheme 1).



Scheme 1. Observed patterns for metal carboxylates: (A) ionic systems and (B–D) with more covalent and coordinated character.

In our systems, both Na^+ and Ca^{2+} cations are present [114]. First, the compounds containing formic and acetic acid dimers without coordinated water or hydrated dimers are considered.

Anhydrous calcium and sodium formates (Figure 7) contain two perpendicular COO^- groups. This arrangement of atoms allows minimization of repulsion between negative oxygen atoms.

In our systems containing superplasticizer, carbon nanotubes and cement components, both Na^+ and Ca^{2+} cations are present. In the subsequent stage of modeling, first their anhydrous salts of formic and acetic acids and then the hydrates are considered.

Anhydrous calcium and sodium formate dimers (Figure 7) show two COO^- groups which are oriented perpendicularly to each other to minimize repulsion of negatively charged oxygen atoms.

A more realistic model of calcium and sodium formate should contain solvent in their first hydration sphere. Taking into account available coordination numbers (CNs) of calcium (from 4 to 9 [114]), we arbitrarily chose the structure with CN = 6 and 7. Therefore, three water molecules could be located in the first hydration shell. The B3LYPD3BJ/aug-cc-pVTZ-optimized structure of $\text{Ca}(\text{OOCCH}_3)_2(\text{H}_2\text{O})_3$ in the gas phase is shown in Figure 8. Water molecules are additionally stabilized by a network of H bonds which also include a water donor hydrogen atom and acid oxygen as a proton acceptor ($\text{H}_d \dots \text{O}_{\text{acid}}$). The calculated H bond lengths are short (1.97–2.08 Å) and indicate fairly strong interactions. The separation between calcium cation and water oxygen atoms is within a range from 2.43 to 2.49 Å. A typical ionic structure with a calcium atom located between two carboxylic

oxygen atoms of both formate anions is predicted with $\text{Ca} \cdots \text{O}$ distances from 2.35 to 2.47 Å.

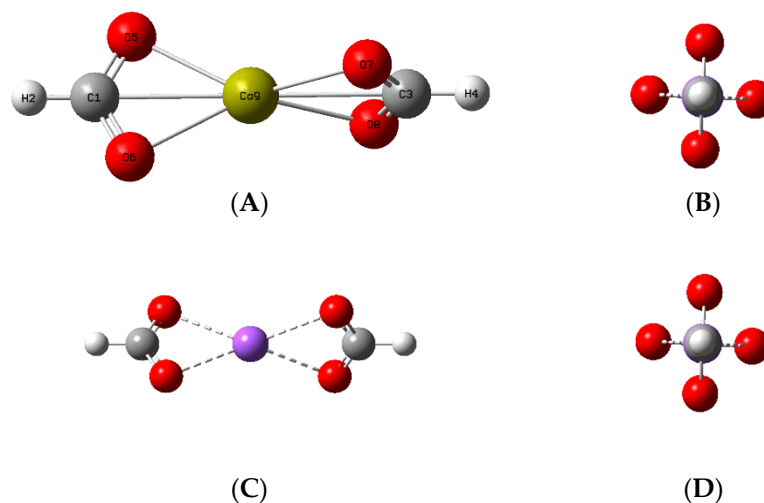


Figure 7. Side (A) and top (B) view of BLYPD3BJ/aug-cc-pVTZ structure of calcium (neutral complex) and sodium formate ((C,D), total charge = -1).

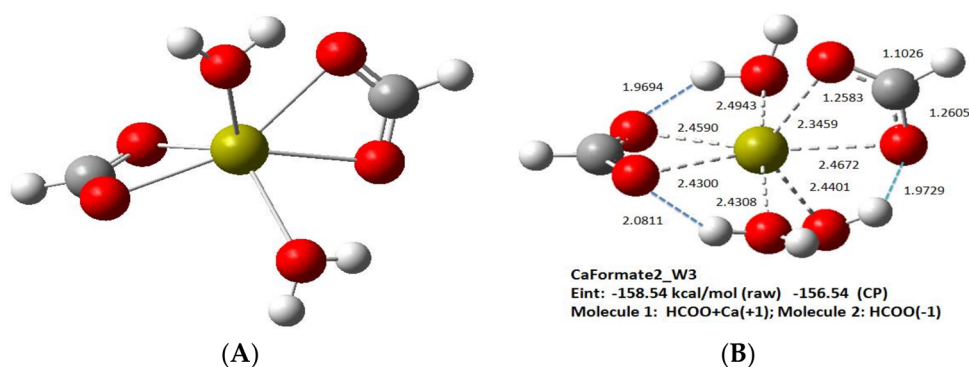


Figure 8. B3LYPD3BJ/aug-cc-pVTZ structure of calcium formate with (A) two and (B) three water molecules (aug-cc-pVTZ-X2C basis set for calcium).

In the case of superplasticizer, which contains both protonated and deprotonated carboxylic groups and sodium cations, we could expect formation of mixed dimers and salts. Using formic acid as a simple model, structures of mixed formic acid–formate anion (Figure 8B) and mixed sodium formate salt were optimized (Figure 9). The first structure indicates a typical symmetric dimer with a hydrogen atom shared by both formate groups. The $\text{O} \cdots \text{H} \cdots \text{O}$ bridges are very short and strong (1.2313 Å). Thus, the raw and CP-corrected interaction energies are -49.84 and -49.60 kcal/mol.

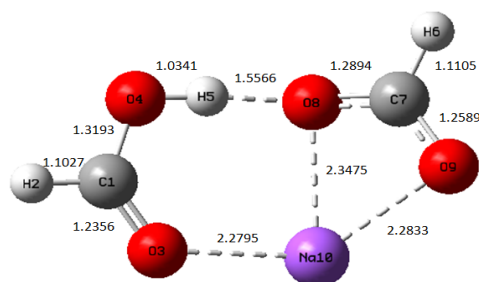


Figure 9. BLYPD3BJ/aug-cc-pVTZ structure of mixed sodium formate salt.

In the case of mixed salt, a strong H bond between the H5 atom of formic acid and the O8 atom of the formate anion is also formed (1.56 Å). The sodium cation is closely connected to three oxygen atoms (O9, O8 and O3 with separations of 2.28, 2.28 and 2.35 Å).

Calcium hydroxide is a type of small molecule, which are very important for cement chemistry. It is a linear molecule but some earlier DFT calculations reported an angle of O-Ca-O smaller than 180 degrees [115]. The B3LYP/6-311++G(3df,3pd) bonds and O-Ca-O angle are 2.038, 0.953 Å and 170°, respectively. However, the MP2 results indicated a linear structure with bonds of 2.046 and 0.953 Å. The mentioned discrepancies are due to the fact that Ca(OH)₂ is a very computationally demanding chemical compound [116].

To clarify the above results, we optimized the calcium hydroxide structure using density functional B3LYP and compared it with our high-level coupled cluster results. The optimized linear structure of Ca(OH)₂, calculated with the all-electron (*ae*) CCSD(T) method, combined with the aug-cc-pVTZ basis set for O and H atoms and aug-cc-pVTZ-X2C for Ca, is shown in Figure 10. Interestingly, in our study, the B3LYP with the same basis sets predicted very similar bond lengths (2.0298 and 0.9533 Å) of the linear molecule with all positive harmonic frequencies. Ca(OH)₂ was additionally optimized with larger and more flexible basis sets (aug-cc-pVQZ, aug-cc-pwCVQZ and aug-cc-pwCVQZ-X2C for H, O and Ca atoms) using SCF-HF, B3LYP and MP2 methods. These calculations also resulted in linear structures with all positive wavenumbers and CaO and OH bond lengths of 2.0461 and 0.9322, 2.0298 and 0.9533, 2.0209 and 0.9526 Å, respectively.



ae CCSD(T) calculated Ca(OH)₂
with aug-cc-pVTZ for O,H and aug-cc-pVTZ-X2C for Ca

Figure 10. Fully optimized linear ae CCSD(T)/aug-cc-pVTZ structure of Ca(OH)₂.

However, the B3LYP/aug-cc-pVTZ calculations resulted in a slightly non-linear molecule with Ca-O-H and O-Ca-O angles of 179.29 and 176.88° and Ca-O and O-H bond lengths were 2.0352 and 0.9547 Å, respectively. In addition, one negative frequency was observed (-53.03 cm^{-1}), indicating the presence of transition (TS) instead of a ground state. In conclusion, our DFT, MP2 and CCSD(T) values are close to benchmark CCSD(T)/aug-cc-pwCVQZ results reported by Radom and coworkers (2.036 and 0.952 Å) [116].

2.3.4. BLYPD3BJ Modeling of Superplasticizer Fragment Structures

A superplasticizer, in particular the polycarboxylate type, acts as the surfactant in cement paste, but it could also significantly improve mixing of nanocarbon material with water. Its action is directly related to its molecular structure, partly reflected in the corresponding IR and Raman spectra (see Figures 2 and 4A).

However, due to the large size of polymeric superplasticizer molecules, we arbitrarily selected (and named) three distinct structural fragments for subsequent theoretical analysis:

- (A) Acid (14 atoms),
- (B) Salt (a carboxylate anion, 13 atoms),
- (C) Ester (24 atoms).

These structures contain two methyl groups representing the main polymeric chain. The molecules of acid, salt and ester shown below were fully optimized at the B3LYP/aug-cc-pVTZ level of theory (see Figure 11).

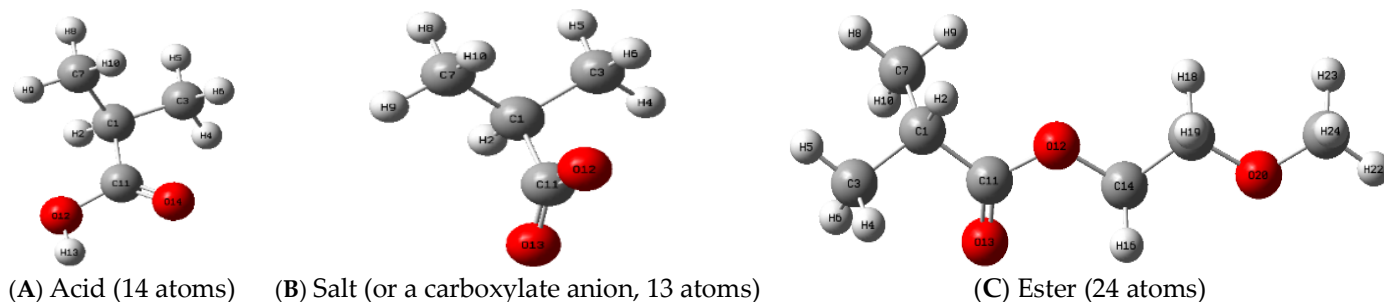


Figure 11. Optimized models of superplasticizer building blocks: (A) Acid, (B) Salt (or a carboxylate anion) and (C) Ester.

It is worth mentioning that, in recent studies, direct interactions between formic acid dimer and (6,6) and (8,8) SWCNTs using DFT and MP2 calculations were reported [108]. However, the authors modeled a small molecule (formic acid dimer) confined inside the carbon nanotube. It was observed that, in the case of intermolecular interactions with graphene-based materials, the model size had no significant effect on energy value [117]. For this reason, it is likely that the interactions of the SWCNTs with small SP models will not significantly affect the quality of the obtained results and their interpretation.

2.3.5. Structure of Model Zigzag (5,0) SWCNT-COOH

Due to the complexity of modeling multi-walled carbon nanotubes, a single-walled nanotube model was used in this work. It is worth noting that in the context of the interaction of the mentioned nanomaterial with a superplasticizer, hydrophilic substituents play a key role, so replacing the MWCNT by an SWCNT does not significantly affect the quality of the obtained results. In the case of fairly large carbon nanotubes, containing 76 atoms, to decrease the computational demands, we reduced the size of the basis set from aug-cc-pVTZ to 6-311++G**. Side and top views of a fully optimized B3LYPD3BJ/6-311++G** zigzag (5,0) SWCNT structure, substituted with single carboxyl groups at both ends, are shown in Figure 12. Additionally, all free valences at both ends of the SWCNT are capped with hydrogen atoms.

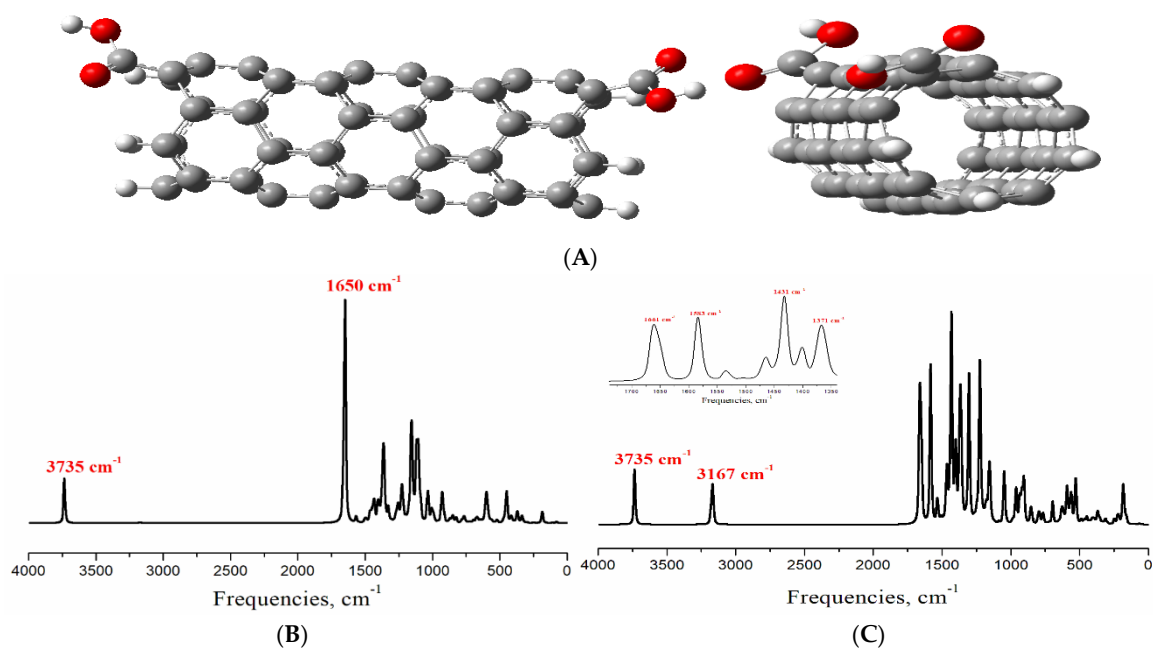


Figure 12. (A) Optimized B3LYPD3BJ/6-311++G** structure of model fragment of zigzag (5,0) SWCNT-COOH composed of five "belts" and the predicted (B) IR and (C) Raman spectra.

Additionally, the corresponding theoretical IR and Raman spectra, predicted for the model SWCNT-COOH molecule, are also shown in Figure 12B and 12C, respectively. Unfortunately, the quality of experimental IR spectra of SWCNT-COOH is low and not suitable for a meaningful comparison (Figure S1). For easier comparison with the experiment (see Figure 5B), the Raman spectrum in Figure S5 is plotted using 20 cm^{-1} line broadening. For brevity, the theoretical Raman spectrum of this model is also shown in Figure 12C with default line broadening of 4 cm^{-1} preserved. The theoretical Raman spectrum clearly indicates bands due to -COOH vibration at 3735 cm^{-1} and asymmetric stretch CH at about 3267 cm^{-1} . In addition, the predicted C=C vibrations at 1583 and 1371 cm^{-1} of the SWCNT model are present in the range of G and D bands observed in our recorded Raman spectra (compare Figures 4B and 13). However, the contribution ratio of -COO^- groups in real samples is significantly smaller than that from the aromatic rings. Thus, in experimental spectra aromatic carbon fragments vibrations dominate.

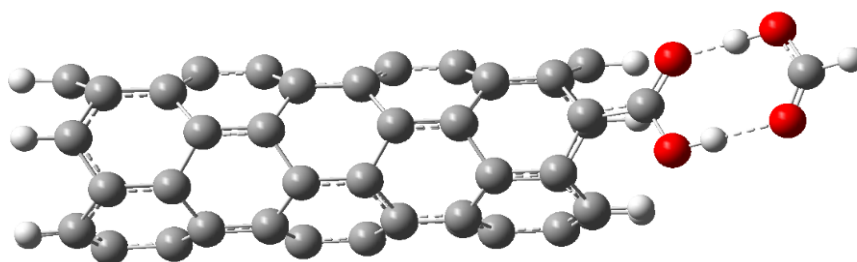


Figure 13. Optimized B3LYP/6-31+G* structure of model fragment of zigzag (5,0) SWCNT-COOH interacting with HCOOH.

2.3.6. Model Zigzag (5,0) SWCNT-COOH Interaction with a Carboxylic Acid

As shown in the previous sections, the -COOH functional groups could strongly bind with polar fragments of superplasticizer and subsequently wrap it around the SWCNT (see Figure 1). Thus, in the theoretical stage of our study we modeled H bond type interaction between our model of a functionalized carbon nanotube and formic acid. The latter compound is selected as the smallest but feasible for calculation model of superplasticizer (Figure 13). Nevertheless, such calculations for a molecular system containing 76 atoms were fairly demanding. Thus, we significantly limited the basis set size and used the Pople type 6-31+G* one. As a result of the calculations, a stable structure was obtained (Figure 13).

In order to estimate the interaction energy of this model, we performed additional single-point counterpoise calculations. As expected, the raw and CP-corrected energies were about -21.98 and -20.63 kcal/mol , respectively. This result supports a strong interaction between the functionalized single-walled carbon nanotube and superplasticizer.

In real samples of superplasticizer and MWCNTs, the H bond interaction takes place for a large number of -COOH groups and the total interaction energy is significantly higher. These interactions result in the formation of stable SP-MWCNT complexes with a specific spatial arrangement. In this case, lone SP hydrophilic groups do not contribute to intramolecular bonds and become more accessible for interactions with the environment. Thus, our theoretical model supports strong interactions between SP and MWCNT-COOH that result in improved mixing with water.

2.4. Biological Tests

Descriptive statistics for the PSII photosynthetic activity of the two moss species are summarized in Table 4.

Table 4. Basic statistical parameters of photosynthetic activity values of bryophytes.

Species	Sample	Mean	Median	Min–Max	Geom. Mean	Harmonic Mean	SD	Variance	Range	Skewness	Kurtosis	Sum
<i>Pf</i>	Control	0.614	0.670	0.147–0.747	0.590	0.552	0.142	0.020	0.600	−1.60	1.88	49.7
	Cement	0.695	0.724	0.218–0.796	0.687	0.673	0.087	0.008	0.578	−3.43	13.7	56.3
	MWCNT-Cement	0.696	0.721	0.358–0.761	0.691	0.685	0.074	0.005	0.403	−2.38	5.97	56.4
<i>Pp</i>	Control	0.602	0.664	0.142–0.740	0.564	0.499	0.162	0.026	0.598	−1.81	2.44	48.7
	Cement	0.471	0.492	0.135–0.746	0.417	0.353	0.200	0.040	0.611	−0.365	−1.20	38.2
	MWCNT-Cement	0.554	0.621	0.130–0.766	0.510	0.448	0.182	0.033	0.636	−1.00	−0.181	44.9

Data presented in Table 4 show the variation in values between samples and species. Figure 14 shows substrate influence on both species’ photosynthetic activity.

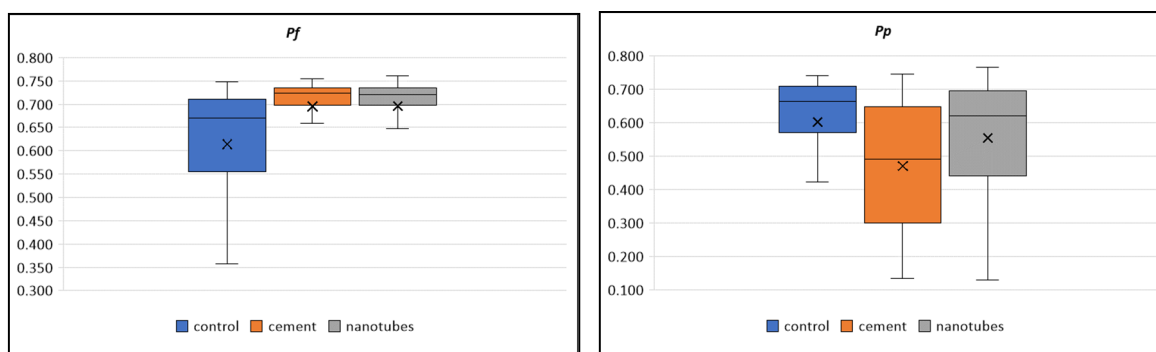


Figure 14. Comparison of photosynthetic activity between individual samples in the species *Polytrichum formosum* (*Pf*) and in the species *Pseudoscleropodium purum* (*Pp*).

The statistical significance of these values is presented in Table 5 and it shows differences between samples within and between species.

Table 5. Statistically significant differences between substrate types and their effect on PSII values (non-parametric Mann–Whitney U test) ^a.

Data	Sum.Rang	Sum.Rang	U	Z	p	Z Correct.	p
<i>Pf</i>							
Control vs. cement	4895	8308	1574	−5.71	***	−5.72	***
Control vs. MWCNT-cement	4944	8259	1623	−5.55	***	−5.55	***
Cement vs. MWCNT-cement	6643	6560	3239	0.137	0.891	0.137	0.891
<i>Pp</i>							
Control vs. cement	7918	5285	1964	4.41	***	4.41	***
Control vs. MWCNT-cement	7100	6104	2783	1.67	0.096	1.67	0.096
Cement vs. MWCNT-cement	5769	7434	2448	−2.79	**	−2.79	**
<i>Pf</i> vs. <i>Pp</i>							
Control vs. cement	6729	6474	3153	0.425	0.671	0.425	0.671
Control vs. MWCNT-cement	9035	4168	847	8.15	***	8.15	***
Cement vs. MWCNT-cement	8588	4615	1294	6.65	***	6.65	***

^a Bold values indicate statistical significance at the level of: ** $p < 0.01$, *** $p < 0.001$.

As can be seen from Table 5, data for both species within different substrates and between species show different statistical significances based on the kind of substrate. For

the moss “Pf”, data from control conditions differ from the other substrate types. However, there are no statistically significant differences between cement vs. MWCNT-cement composites. In the case of Pp moss, the relationship is slightly different. In particular, the type of substrate, e.g., cement vs. MWCNT-cement, influences statistically significant differences in the PSII photosynthetic activity values of the species. The difference is also apparent from the comparison of these values between the species, where we can also see differences at the $p < 0.001$ level between cement and Pf vs. cement and Pp and carbon nanotubes and Pf vs. carbon nanotubes and Pp.

Environmental factors have an important influence on the plant (including moss) life cycle [118]. For example, the impact of temperature and light intensity can directly influence the chlorophyll content, the photosynthetic rate in mosses and thus photosynthetic activity, e.g., in peat mosses [119,120]. The type of substrate used also plays a key role in the growth and development of mosses [121]. As shown in Table 4 and Figure 14, both species, depending on the substrate, showed variable photosynthetic activity during the two-month-long experiment. The fact that the mosses maintain their vitality may be related to their entry into cryptobiosis. Throughout their life cycle they are able to vegetate in this way for a very long time [122]. The established cut-off value is 0.1 [123]. Below this value, mosses should only be considered as a natural pollutant sorbent and not as a living bioindicator and organism. As indicated by the results of our analyses, no values < 0.1 were recorded during the study period. However, there is a noticeable difference between species (see Figure 14), as confirmed by a statistically significant difference (Table 5). This indicates a variable adaptation mechanism of each species to a change in living conditions (transfer from natural ecosystem to artificial conditions). Despite the provision of relatively constant conditions for functioning (humidity, light intensity, photoperiod), the mosses were characterized by variable photosynthetic activity, which may reflect the individual response of each moss during the measurements. Differences are seen relative to the used substrates on which mosses live.

3. Experimental

3.1. Materials

In this study, we used a commercial polycarboxylate superplasticizer (BASF, see Figure S6) (“Master Glenium ACE 420” as 30% solution in distilled water) as a surfactant to form a homogeneous mixture of multi-walled carbon nanotubes (MWCNTs). Raw multi-walled carbon nanotubes (MWCNTs) with the trade name CTUBE 100 from CNT Co., Ltd. (Suwon-si, Republic of Korea, provided in 2015) were used (see Figure 15).

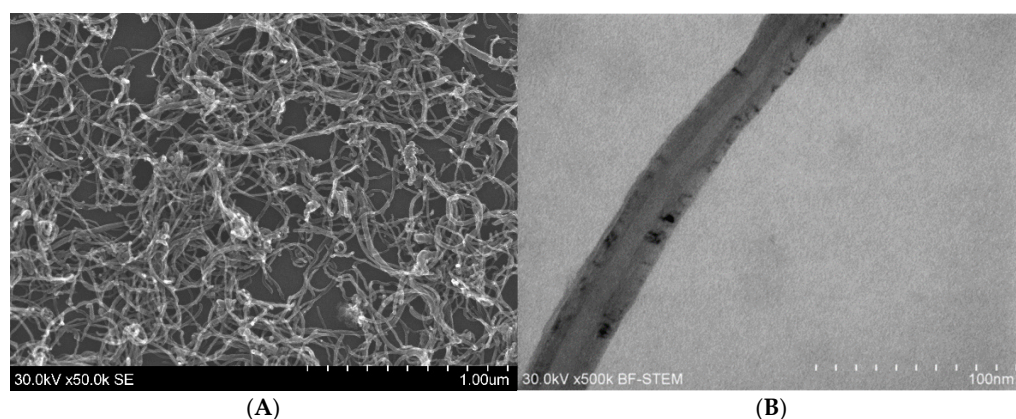


Figure 15. TEM image of (A) bundled MWCNTs and (B) enlarged fragment of MWCNT.

The nanotubes were synthesized by thermal vapor deposition (thermal CVD) and characterized by several techniques, including TEM, SEM, elemental analysis, EDX, FT-IR, Raman spectroscopy and electron spectroscopy methods [39]. The diameter of the used MWCNTs was from 20 to 40 ± 10 nm and their length from 1 to 10 μm [39] (see Figure 15A

showing TEM image of bundled MWCNTs and an enlarged fragment of a single tube in Figure 15B). Thus, MWCNTs were characterized by a large length-to-diameter ratio and their ends were carboxylated which facilitated their binding to cement grains via formation of MWCNT-COO⁻ - - Ca²⁺- (cement grain) ionic bonding [55] and non-covalent hydrogen bonds of -COOH - - - HO- (cement grain). This leads to long, bundled “anchor” nanotubes and bridging small cracks. The used multi-walled carbon nanotubes were carboxylated (MWCNT-COOH) mainly at their ends. However, for convenience, in the following parts of the study we refer to them as MWCNTs.

Cement composites for biological tests were prepared using CEM I 42.5 R (CEM I) cement from Odra Cement Plant in Opole (Poland).

3.2. Biological Materials

Two moss species were used in the biological study: *Polytrichum formosum* Hedw. (Pf) and *Pseudoscleropodium purum* (Limpr) M. Fleisch. ex Broth. (Pp). Plant material was collected at the beginning of July 2024 from forests in Opole Voivodeship in the Bory Niemodlińskie region of the Prószków Forest District near the cities of Prószków and Jaśkowice (N50.581981, E17.825761 and N50.582360, E17.825151). Mosses were sampled in open areas, at least three meters from the nearest tree crown, from the ground, according to the ICP Vegetation protocol guidelines [124]. The collected samples were transported to the laboratory using the transplant method [125].

3.3. Methods

3.3.1. Preparation of Suspensions of MWCNTs in the Superplasticizer

In general, it is not easy to prepare a uniform mixture of carbon nanomaterial and cement. As result of several tests, we decided to first make a homogeneous mixture of MWCNTs in liquid superplasticizer (see Figure S7). In other words, a kind of mechano-chemical method was used to make a homogenous mixture of partly hydrophobic carbon nanotubes in a water environment. A three-roll mill (EXAKT 80S) was used to prepare suspensions of carbon nanomaterials in the superplasticizer. The grinding process was carried out with a minimum gap of 5 µm between the rolls. This process was carried out until a homogeneous suspension was obtained (after three rolling cycles).

A suspension of MWCNTs in superplasticizer was prepared with the above method. FT-IR and Raman characterization was performed for the superplasticizer (SP) and SP + 3% wt. MWCNTs.

3.3.2. FT-IR Spectroscopy

The applied superplasticizer was studied using FT-IR spectroscopy in the form of a thin liquid film between two KBr pellets. It was possible to measure samples of MWCNTs suspended in SP in the form of KBr pellets (5 mg/500 mg KBr, like for typical IR measurements of solid state samples). All FT-IR spectra were obtained in the range of 4000 to 400 cm⁻¹ using a Thermo Nicolet Nexus spectrometer and with a resolution of 2 cm⁻¹.

In addition, for fast characterization of the studied samples, the attenuated transmission reflectance (ATR) spectra were also recorded. The ATR spectra show the main features of FT-IR spectra though their resolution is significantly lower (close signals are more overlapped with slightly shifted peak positions).

3.3.3. Raman Spectroscopy

A Raman confocal Alpha 300R microscope with an Olympus 50x/0.50 long working distance objective was used to collect spectra in the spectral window of 150–4000 cm⁻¹. The laser beam with a wavelength of 532 nm and a power of 1.5 mW was focused on a small area of the sample and the Raman signal, recorded with a 1s acquisition time, was acquired 200 times.

Raman spectra were measured from small amounts of oily and very thick liquid superplasticizer and its suspension containing 3% MWCNTs.

A flat baseline and good-quality spectrum of superplasticizer (with high signal-to-noise ratio) was observed. However, the addition of MWCNTs resulted in strong fluorescence of the sample and the spectra were recorded with a highly raised baseline. Thus, to obtain meaningful spectra it was necessary to perform digital baseline correction prior to analysis.

3.4. Computational Details

All calculations were performed using the Gaussian 16 C.01 program [126]. Obviously, the size of a real system is too big for molecular modeling and, therefore, the selection of smaller but reasonable models is essential [62]. It was also important to choose proper theoretical tools [62]. Due to its efficiency in predicting accurate structures, energies and spectroscopic parameters, we selected DFT and applied the B3LYP hybrid density functional [42,127–129]. In addition, in some cases we also used an older, “pure” density functional—BLYP [127,130]. In our earlier works we noticed that this functional works somewhat faster and provides improved vibrational frequencies but predicts slightly less accurate geometry [131,132]. Models of superplasticizer and carbon nanotubes, selected for calculations, are fairly large. Thus, we decided to start an unconstrained optimization of geometry with a very small basis set, 3–21G, first and subsequently used larger ones (6-31G*, 6-311++G** and in some cases also aug-cc-pVTZ, subsequently abbreviated as aVTZ) [62,133–136]. It should be noticed that due to the presence of multiple bonds and lone electron pairs in structures of our models, the use of basis sets containing both polarization and diffuse functions is essential [62,133–136]. Additionally, to account for weak long-range dispersion interactions we also implemented the recently introduced Grimme’s empirical term GD3 [137] with Becke–Johnson dumping correction BJ [138].

In order to verify the selection of two density functionals and empirical correction of dispersion, we initially checked their performance on two small molecules and their homodimers—water and formic acid. In the next step, we modeled the structure and H bonding interactions between the two simplest protonated and deprotonated carboxylic acids and their interactions with sodium and calcium cations. Finally, we analyzed the interactions between fragments of carboxylated single-walled carbon nanotubes and fragments of superplasticizer molecule. Obviously, the use of the MWCNT model is significantly more computationally expensive and therefore it was not modeled in the current study.

3.5. Composite Preparation for Biological Studies

Cement composites for biological tests were prepared and their composition is shown in Table 6.

Table 6. Compositions (in g) of studied cement probes.

Composite	CEM I	Water	MWCNT-SP
Cement	250	300	-
MWCNT-Cement	250	300	2.75

3.6. Biological Studies

In the laboratory, mosses were re-identified to ensure species homogeneity, using a SZ61 microscope (Olympus, Tokyo, Japan) and an IPOS-810 (Delta Optical, Gdańsk, Poland). The process was carried out in the research section of the International Research and Development Center of the University of Opole (MCBR UO). The experiment was conducted in the FITO-R phytotron rack (Biogenet Ltd., Gdańsk, Poland) in the MCBR UO building (see Figure S8). Mosses were cultured on three types of substrate: control (3 cm layer of sterile sand), hardened cement paste (3 cm layer), hardened MWCNT-modified cement paste (3 cm layer). Culture conditions, including maintaining the appropriate temperature of 21 °C and humidity of 50%, were determined according to the literature [139].

In order to assess the effect of substrate type on the viability of mosses—photosystem II chlorophyll fluorescence (PSII)—the actual photochemical productivity (yield) [140] was measured using a modulated portable fluorometer (Opti-Sciences, Hudson, NH, USA) under ambient light conditions [141]. PSII was measured three times a week for a period of two months from 12 July to 14 September 2024. For each species and each substrate variant, three measurements were taken (81 measurements). A total of 486 measurements were taken.

Statistical analysis of the results obtained was performed using Microsoft Excel 2021 and STATISTICA (version 13.3) software for data processing and visualization. For descriptive analysis, basic descriptive statistics values (min, max, median, mean with standard deviation, variance, skewness, kurtosis and sum) were calculated for photosynthetic activity data across variants (Table 4). The significance of differences between species and substrates was ensured by independent pooled sampling [142]. The normality of the data was tested using the Shapiro–Wilk test. To avoid significant differences between photosynthetic activity values leading to non-normal distribution of the data, a Box–Cox transformation was applied to improve and increase the normality of the data [143]. Lacking such improvement in terms of obtaining a normal distribution, differences between photosynthetic activity values were assessed using the non-parametric Mann–Whitney U statistical test. A difference was considered statistically significant when $p < 0.05$.

4. Conclusions

Mixing nanocarbon structures with cement paste to obtain homogenous mixtures is a very difficult process. It was demonstrated in the current study that a simultaneous blending of MWCNTs with polycarboxylated superplasticizer using an efficient mixing mill could produce a well-dispersed suspension, which is suitable for easier addition to cement. FT-IR and Raman spectroscopy were used to characterize a superplasticizer and suspension of MWCNTs with SP in a water environment. The experimental findings were supported by theoretical modeling of interactions between fragments of polymeric superplasticizer (acid, salt and esters) and functionalized carbon nanotubes. The density functional theory was applied to obtain structural and energetic parameters of the fully optimized models. The BLYP and B3LYP density functionals combined with reasonable size basis sets predicted reliable structures and IR/Raman vibrational spectra of interacting molecules (water, formic and acetic acids and their dimers).

Finally, the finite models of SWCNT-COOH carbon nanotubes were also built and their interaction with formic acid representing the superplasticizer was assessed. The estimated counterpoise-corrected interaction energy between H bonded SWCNT-COOH and HCOOH was about -21 kcal/mol. Such a significant interaction supports the presence of a strong interaction between “interaction hot spots” of nanotubes with a polymeric SP molecule, which leads to better mixing with a polar environment (water). The obtained theoretical results could improve our understanding about the formation of well-dispersed nanocarbon material in a superplasticizer leading to easier introduction of SWCNTs (and MWCNTs) to cement paste and concrete mix.

As result of the conducted biological studies, no clear effect of the cement substrate with the addition of MWCNTs on the studied moss species’ vitality was observed. In the case of *Polytrichum formosum*, composite modification did not induce a statistically significant effect. However, notable vitality changes of *Pseudoscleropodium purum* were observed. It should be concluded that the effect of the cement paste with the addition of MWCNTs is not clear-cut and will depend on the adaptability of the individual moss species. However, the addition of nanoparticles did not have a negative effect on the functioning of the species *Polytrichum formosum* and *Pseudoscleropodium purum*. Moreover, higher *Pseudoscleropodium purum* PSII activity on MWCNT-cement was observed compared to the control substrate. The obtained results confirmed the hypothesis that mosses could be used as bioindicators of nanomodified building materials’ environmental effect. Cement paste with MWCNTs does not have a destructive effect on the studied mosses’ viability.

Supplementary Materials: The following supporting information can be downloaded at: <https://www.mdpi.com/article/10.3390/molecules29225379/s1>, Figure S1: FTIR spectra of MWCNT; Figure S2: BLYPD3BJ and B3LYPD3BJ (in parenthesis) optimized structures of linear water dimer (the aug-cc-pVTZ basis set was used, distances are in Å, angles in degrees and interaction energy in kcal/mol); Figure S3: BLYPD3BJ and BLYP (in parenthesis) optimized structures of (A) *trans*-formic and (B) *trans*-acetic acid monomers (the aug-cc-pVTZ basis set was used, distances are in Å); Figure S4: BLYPD3BJ/aVTZ and BLYP/aVTZ optimized structures of acetic acid dimer (interatomic distances in Å); Figure S5: The predicted Raman spectrum (20 cm⁻¹ linewidth is used) of optimized BLYPD3BJ/6-311++G** structure of model fragment of zigzag (5,0) SWCNT-COOH composed from five “belts”; Figure S6: Chemical formula of studied superplasticizer; Figure S7: Photos of MWCN-SP (A) before and (B) after mixing; Figure S8: Moss cultivation in phytotron rack on three types of substrate: control, cement composite and MWCNT-modified cement composite; Table S1: DFT predicted (A) structural and vibrational parameters of water monomer using aug-cc-pVTZ basis set and their (B) deviations from experiment. Experimental and benchmark theoretical values are given for comparison (bonds in Å, angle in degrees and wavenumbers in cm⁻¹); Table S2: DFT calculated structural parameters, interaction energy and vibration frequencies of water dimer are compared with experiment and benchmark calculations (distances in Å, angles in degrees, wavenumbers in cm⁻¹ and interaction energy in kcal/mol); Table S3: (A) BLYPD3BJ, BLYP, B3LYPD3BJ and B3LYP optimized bond lengths (in Å) of *trans*-formic and *trans*-acetic acid monomers and (B) the corresponding deviations from experiment. The aug-cc-pVTZ basis set was used. Experimental and benchmark parameters are included for comparison; Table S4: (A) Selected experimental and theoretical benchmark wavenumbers of formic acid monomer, (B) BLYP and BLYPD3BJ and (C) B3LYP and B3LYPD3BJ calculated harmonic and anharmonic values using the aug-cc-pVTZ basis set; Table S5: BLYP, BLYPD3BJ, B3LYP and B3LYPD3BJ calculated harmonic and anharmonic frequencies of acetic acid monomer using the aVTZ basis set; Table S6: BLYP, BLYPD3BJ, B3LYP and B3LYPD3BJ predicted formic acid dimer interatomic distances using aVTZ basis set and their deviations from experiment. Experimental and benchmark parameters are included for comparison; Table S7: Experimental and benchmark frequencies of formic acid dimer; Table S8: BLYP, BLYPD3BJ, B3LYP and B3LYPD3BJ calculated harmonic and anharmonic frequencies of formic acid dimer. aVTZ basis set is used and RMS deviations from experiment are also shown; Table S9: BLYP/aVTZ, BLYPD3BJ/aVTZ, B3LYP/aVTZ and B3LYPD3BJ/aVTZ calculated harmonic and anharmonic frequencies of acetic acid dimer; Table S10: Raw and CP-corrected interaction energy (in kcal/mol) of formic and acetic acid dimers. The magnitude of dispersion and BSSE is also evaluated, see refs. [144,145].

Author Contributions: T.K.: writing—original draft, conceptualization, methodology. N.M.: writing—original draft, theoretical investigation, data analyses and visualization. P.Ś.: writing—original draft, methodology, biological test investigation, data curation and visualization. M.R.: writing—review and editing, methodology, biological test investigation, data curation and visualization. A.M.: preparation of carbon nanomaterials and experimental investigation. L.S.: preparation of carbon nanomaterials and experimental investigation. S.G.: writing—review and editing and conceptualization. K.J.: experimental investigation and data analysis. A.S.: investigation, analysis and visualization of IR data. R.W.: investigation and visualization of spectroscopic data. O.R.: writing—review and editing. K.E.: writing—review and editing. All authors have read and agreed to the published version of the manuscript.

Funding: S.G. and K.J. were partly supported by Opole University of Technology. T.K., N.M. and K.E. were partly supported by the University of Opole. R.W. was partly supported by the University of Silesia. This work was carried out at International Research and Development Center of the University of Opole (MCBR UO), which was established as part of a project co-financed by the European Union under the European Regional Development Fund, RPO WO 2014-2020, Action 1.2 Infrastructure for R&D. Agreement No. RPOP.01.02.00-16-0001/17-00 dated 31 January 2018.

Institutional Review Board Statement: Not applicable.

Informed Consent Statement: Not applicable.

Data Availability Statement: Data are contained within the article and Supplementary Materials.

Acknowledgments: Created using resources provided by Wrocław Centre for Networking and Supercomputing (<http://wcss.pl>). Grant no. hpc-teobald-1713867719.

Conflicts of Interest: The authors declare no competing interests.

References

1. Bastos, G.; Patiño-Barbeito, F.; Patiño-Cambeiro, F.; Armesto, J. Nano-Inclusions Applied in Cement-Matrix Composites: A Review. *Materials* **2016**, *9*, 1015. [[CrossRef](#)] [[PubMed](#)]
2. Sobolev, K.; Flores, I.; Torres-Martinez, L.M.; Valdez, P.L.; Zarazua, E.; Cuellar, E.L. *Engineering of SiO₂ Nanoparticles for Optimal Performance in Nano Cement-Based Materials*; Nanotechnology in Construction 3; Bittnar, Z., Bartos, P.J.M., Němeček, J., Šmilauer, V., Zeman, J., Eds.; Springer: Berlin/Heidelberg, Germany, 2009; pp. 139–148.
3. Kong, D.; Su, Y.; Du, X.; Yang, Y.; Wei, S.; Shah, S.P. Influence of nano-silica agglomeration on fresh properties of cement pastes. *Constr. Build. Mater.* **2013**, *43*, 557–562. [[CrossRef](#)]
4. Sikora, P.; Horszczaruk, E.; Cendrowski, K.; Mijowska, E. The Influence of Nano-Fe₃O₄ on the Microstructure and Mechanical Properties of Cementitious Composites. *Nanoscale Res. Lett.* **2016**, *11*, 182. [[CrossRef](#)] [[PubMed](#)]
5. Sobolkina, A.; Mechtcherine, V.; Khavrus, V.; Maier, D.; Mende, M.; Ritschel, M.; Leonhardt, A. Dispersion of carbon nanotubes and its influence on the mechanical properties of the cement matrix. *Cem. Concr. Compos.* **2012**, *34*, 1104–1113. [[CrossRef](#)]
6. Zhou, C.; Li, F.; Hu, J.; Ren, M.; Wei, J.; Yu, Q. Enhanced mechanical properties of cement paste by hybrid graphene oxide/carbon nanotubes. *Constr. Build. Mat.* **2017**, *134*, 336–345. [[CrossRef](#)]
7. Zuo, J.; Yao, W.; Wu, K. Seebeck Effect and Mechanical Properties of Carbon Nanotube-Carbon Fiber/Cement Nanocomposites. *Fuller. Nanotub. Carbon Nanostruct.* **2015**, *23*, 383–391. [[CrossRef](#)]
8. Metaxa, Z.S.; Seo, J.T.; Konsta-Gdoutos, M.S.; Hersam, M.C.; Shah, S.P. Highly concentrated carbon nanotube admixture for nano-fiber reinforced cementitious materials. *Cem. Concr. Compos.* **2012**, *5*, 612–617. [[CrossRef](#)]
9. Xu, T.; Yang, J.; Liu, J.; Fu, Q. Surface modification of multi-walled carbon nanotubes by O₂ plasma. *Appl. Surf. Sci.* **2007**, *253*, 8945–8951. [[CrossRef](#)]
10. Mohamadian, N.; Ramhormozi, M.Z.; Wood, D.A.; Ashena, R. Reinforcement of oil and gas wellbore cements with a methyl methacrylate/carbon-nanotube polymer nanocomposite additive. *Cem. Concr. Compos.* **2020**, *114*, 103763. [[CrossRef](#)]
11. Zhang, Z.-Y.; Xu, X.-C. Nondestructive covalent functionalization of carbon nanotubes by selective oxidation of the original defects with K₂FeO₄. *Appl. Surf. Sci.* **2015**, *346*, 520–527. [[CrossRef](#)]
12. Chen, J.; Yao, B.; Li, C.; Shi, G. An improved Hummers method for eco-friendly synthesis of graphene oxide. *Carbon* **2013**, *64*, 225–229. [[CrossRef](#)]
13. Chelmecka, E.; Pasterny, K.; Kupka, T.; Stobiński, L. DFT studies of COOH tip-functionalized zigzag and armchair single wall carbon nanotubes. *J. Mol. Model.* **2012**, *18*, 2241–2246. [[CrossRef](#)] [[PubMed](#)]
14. Chelmecka, E.; Pasterny, K.; Kupka, T.; Stobinski, L. OH-functionalized open-ended armchair single-wall carbon nanotubes (SWCNT) studied by density functional theory. *J. Mol. Model.* **2012**, *18*, 1463–1472. [[CrossRef](#)] [[PubMed](#)]
15. Dresselhaus, M.S.; Dresselhaus, G.; Saito, R.; Jorio, A. Raman spectroscopy of carbon nanotubes. *Phys. Rep.* **2005**, *409*, 47–99. [[CrossRef](#)]
16. Dresselhaus, M.S.; Dresselhaus, G.; Jorio, A. Raman spectroscopy of carbon nanotubes in 1997 and 2007. *J. Phys. Chem. C* **2007**, *111*, 17887–17893. [[CrossRef](#)]
17. Colthop, N.B.; Daly, L.H.; Wiberley, S.E. *Introduction to Infrared and Raman Spectroscopy*; Academic Press Inc.: New York, NY, USA; London, UK, 1965.
18. Vogel, I. *Chemistry Including Qualitative Organic Analysis*; Longman Group Ltd.: London, UK, 1979.
19. Alpert, N.L.; Keiser, W.E.; Szymanski, H.A. *Infrared Spectroscopy*; PWN: Warszawa, Poland, 1974. (In Polish)
20. Hummel, D.O.; Scholl, F.K. *Atlas of Plastics Additives—Analysis by Spectrometric Methods*; Springer: Berlin/Heidelberg, Germany; New York, NY, USA, 2002.
21. Hummel, D.O.; Scholl, F.K. *Atlas of Polymer and Plastics Analysis, Volume 2—Plastics, Fibres, Rubbers, Resins—Spectra and Methods of Identification*; Carl Hanser: Munchen, Germany; Weinheim, Germany, 1990.
22. Hummel, D.O.; Scholl, F.K. *Atlas of Polymer and Plastics Analysis, Volume 3—Additives and Processing Aids*; Carl Hanser: Munchen, Germany; Weinheim, Germany, 1990.
23. Hummel, D.O.; Scholl, F.K. *Atlas of Polymer and Plastics Analysis. 2. Vol. 1. Polymers: Structures and Spectra*; Chemie: Weinheim, Germany; Carl Hanser: München, Germany, 1978; Volume XXXII, 671p.
24. Bokobza, L.; Zhang, J. Raman spectroscopic characterization of multiwall carbon nanotubes and of composites. *EXPRESS Polym. Lett.* **2012**, *6*, 601–608. [[CrossRef](#)]
25. Malard, L.M.; Pimenta, M.A.; Dresselhaus, G.; Dresselhaus, M.S. Raman spectroscopy in graphene. *Phys. Rep.* **2009**, *473*, 51–87. [[CrossRef](#)]
26. Tuinstra, F.; Koenig, J.L. Raman Spectrum of Graphite. *J. Chem. Phys.* **1970**, *53*, 1126–1130. [[CrossRef](#)]
27. Wu, J.-B.; Lin, M.-L.; Cong, X.; Liu, H.-N.; Tan, P.-H. Raman spectroscopy of graphene-based materials and its applications in related devices. *Chem. Soc. Rev.* **2018**, *47*, 1822–1873. [[CrossRef](#)]
28. Ouyang, Y.; Cong, L.M.; Chen, L.; Liu, Q.X.; Fang, Y. Raman study on single-walled carbon nanotubes and multi-walled carbon nanotubes with different laser excitation energies. *Phys. E Low Dimens. Syst. Nanostruct.* **2008**, *40*, 2386–2389. [[CrossRef](#)]
29. Ferrari, A.C. Raman spectroscopy of graphene and graphite: Disorder, electron–phonon coupling, doping and nonadiabatic effects. *Solid State Commun.* **2007**, *143*, 47–57. [[CrossRef](#)]

30. Zdrojek, M.; Gebicki, W.; Jastrzebski, C.; Melin, T.; Huczko, A. Studies of Multiwall Carbon Nanotubes Using Raman Spectroscopy and Atomic Force Microscopy. *Solid State Phenom.* **2004**, *99–100*, 265–268. [[CrossRef](#)]
31. Zólyomi, V.; Koltai, J.; Kürti, J. Resonance Raman spectroscopy of graphite and graphene. *Phys. Status Solidi B* **2011**, *248*, 2435–2444. [[CrossRef](#)]
32. Heise, H.M.; Kuckuk, R.; Ojha, A.K.; Srivastava, A.; Srivastava, V.; Asthana, B.P. Characterisation of carbonaceous materials using Raman spectroscopy: A comparison of carbon nanotube filters, single- and multi-walled nanotubes, graphitised porous carbon and graphite. *J. Raman Spectrosc.* **2009**, *40*, 344–353. [[CrossRef](#)]
33. Hodkiewicz, J. *Characterizing Carbon Materials with Raman Spectroscopy. Application Note: 51901*; Thermo Fisher Scientific: Madison, WI, USA, 2010.
34. Ouyang, Y.; Fang, Y. Temperature dependence of the raman spectra of carbon nanotubes with 1064 nm excitation. *Phys. E* **2004**, *24*, 222–226. [[CrossRef](#)]
35. Titus, E.; Ali, N.; Cabral, G.; Gracio, J.; Ramesh Babu, P.; Jackson, M.J. Chemically functionalized carbon nanotubes and their characterization using thermogravimetric analysis, fourier transform infrared, and raman spectroscopy. *J. Mater. Eng. Perform.* **2006**, *15*, 182–186. [[CrossRef](#)]
36. Stobinski, L.; Tomasik, P.; Lii, C.-Y.; Chan, H.-H.; Lin, H.-M.; Liu, H.-L.; Kao, C.-T.; Lu, K.-S. Single-walled carbon nanotube–amylopectin complexes. *Carbohydr. Polym.* **2003**, *51*, 311–316. [[CrossRef](#)]
37. Lii, C.-Y.; Stobinski, L.; Tomasik, P.; Liao, C.-D. Single-walled carbon nanotube—Potato amylose complex. *Carbohydr. Polym.* **2003**, *51*, 93–98. [[CrossRef](#)]
38. Siddique, R.; Mehta, A. Effect of carbon nanotubes on properties of cement mortars. *Constr. Build. Mater.* **2014**, *50*, 116–129. [[CrossRef](#)]
39. Stobinski, L.; Lesiak, B.; Kövér, L.; Tóth, J.; Biniak, S.; Trykowski, G.; Judek, J. Multiwall carbon nanotubes purification and oxidation by nitric acid studied by the FTIR and electron spectroscopy methods. *J. Alloys Compd.* **2010**, *501*, 77–84. [[CrossRef](#)]
40. Hohenberg, P.; Kohn, W. Inhomogeneous Electron Gas. *Phys. Rev.* **1964**, *136*, B864–B871. [[CrossRef](#)]
41. Kohn, W.; Sham, L.J. Self-Consistent Equations Including Exchange and Correlation Effects. *Phys. Rev.* **1965**, *140*, A1133–A1138. [[CrossRef](#)]
42. Becke, A.D. Density-functional thermochemistry. III. The role of exact exchange. *J. Chem. Phys.* **1993**, *98*, 5648–5652. [[CrossRef](#)]
43. Oliveira, A.M.L.; Machado, M.; Silva, G.A.; Bitoque, D.B.; Tavares Ferreira, J.; Pinto, L.A.; Ferreira, Q. Graphene Oxide Thin Films with Drug Delivery Function. *Nanomaterials* **2022**, *12*, 1149. [[CrossRef](#)]
44. Derakhshi, M.; Daemi, S.; Shahini, P.; Habibzadeh, A.; Mostafavi, E.; Ashkarran, A.A. Two-Dimensional Nanomaterials beyond Graphene for Biomedical Applications. *J. Funct. Biomater.* **2022**, *13*, 27. [[CrossRef](#)]
45. Haynes, A.; Popek, R.; Boles, M.; Paton-Walsh, C.; Robinson, S.A. Roadside Moss Turfs in South East Australia Capture More Particulate Matter Along an Urban Gradient than a Common Native Tree Species. *Atmosphere* **2019**, *10*, 224. [[CrossRef](#)]
46. Macedo-Miranda, G.; Avila-Pérez, P.; Gil-Vargas, P.; Zarazúa, G.; Sánchez-Meza, J.C.; Zepeda-Gómez, C.; Tejada, S. Accumulation of heavy metals in mosses: A biomonitoring study. *SpringerPlus* **2016**, *5*, 715. [[CrossRef](#)]
47. Jang, K.; Viles, H. Moisture Interactions Between Mosses and Their Underlying Stone Substrates. *Stud. Conserv.* **2022**, *67*, 532–544. [[CrossRef](#)]
48. Gabrych, M.; Kotze, D.J.; Lehvävirta, S. Substrate depth and roof age strongly affect plant abundances on sedum-moss and meadow green roofs in Helsinki, Finland. *Ecol. Eng.* **2016**, *86*, 95–104. [[CrossRef](#)]
49. Purre, A.-H.; Ilomets, M.; Truus, L.; Pajula, R.; Sepp, K. The effect of different treatments of moss layer transfer technique on plant functional types' biomass in revegetated milled peatlands. *Restor. Ecol.* **2020**, *28*, 1584–1595. [[CrossRef](#)]
50. Perini, K.; Castellari, P.; Giachetta, A.; Turcato, C.; Roccotiello, E. Experiencing innovative biomaterials for buildings: Potentialities of mosses. *Build. Environ.* **2020**, *172*, 106708. [[CrossRef](#)]
51. Pouliot, R.; Hugron, S.; Rochefort, L. Sphagnum farming: A long-term study on producing peat moss biomass sustainably. *Ecol. Eng.* **2015**, *74*, 135–147. [[CrossRef](#)]
52. Redfern, P.; Kupka, T.; Curtiss, L.A. Quantum Chemical Studies of Li Ion Hopping Mechanism in Polymer Electrolytes. *ECS Trans.* **2019**, *3*, 163–167. [[CrossRef](#)]
53. Janowska-Renkas, E. *Budowa Superplastyfikatora a Efektywność jego Wpływu na Właściwości Zaczynu Cementowego (The Structure of a Superplasticizer and the Effectiveness of Its Influence on the Properties of Cement Paste)*; Studia z Zakresu Inżynierii, KILiW PAN: Warszawa, Poland, 2013; p. 82.
54. Janowska-Renkas, E. The influence of the chemical structure of polycarboxylic superplasticizers on their effectiveness in cement pastes. *Procedia Eng.* **2015**, *108*, 575–583. [[CrossRef](#)]
55. Li, Y.; Li, H.; Wang, Z.; Jin, C. Effect and mechanism analysis of functionalized multi-walled carbon nanotubes (MWCNTs) on C-S-H gel. *Cem. Concr. Res.* **2020**, *128*, 105955. [[CrossRef](#)]
56. Ferrari, A.C.; Robertson, J.M.; Zhao, Q.; Wagner, H.D. Raman spectroscopy of carbon-nanotube-based composites. *Philos. Trans. R. Soc. A* **2004**, *362*, 2407–2424.
57. Bounos, G.; Andrikopoulos, K.S.; Karachalios, T.K.; Voyiatzis, G.A. Evaluation of multi-walled carbon nanotube concentrations in polymer nanocomposites by Raman spectroscopy. *Carbon* **2014**, *76*, 301–309. [[CrossRef](#)]

58. Granados-Martínez, F.G.; Contreras-Navarrete, J.J.; Ambriz-Torres, J.M.; Gutiérrez-García, C.J.; García-Ruiz, D.L.; Guzmán-Fuentes, J.A.; Flores-Ramírez, N.; Cisneros-Magaña, M.R.; García-González, L.; Zamora-Peredo, L.; et al. MWCNTs-polymer composites characterization through spectroscopies: FTIR and Raman. *MRS Adv.* **2018**, *3*, 3757–3762. [[CrossRef](#)]
59. Pople, J.A.; Head-Gordon, M.; Raghavachari, K. Quadratic configuration interaction—A general technique for determining electron correlation energies. *J. Chem. Phys.* **1987**, *87*, 5968–5975. [[CrossRef](#)]
60. Benedict, W.S.; Gailar, N.; Plyler, E.K. Rotation-Vibration Spectra of Deuterated Water Vapor. *J. Chem. Phys.* **1956**, *24*, 1139–1165. [[CrossRef](#)]
61. Feller, D.; Peterson, K.A. High level coupled cluster determination of the structure, frequencies, and heat of formation of water. *J. Chem. Phys.* **2009**, *131*, 154306. [[CrossRef](#)] [[PubMed](#)]
62. Foresman, J.B.; Frisch, A. *Exploring Chemistry with Electronic Structure Methods*, 2nd ed.; Gaussian Inc.: Pittsburg, PA, USA, 1996.
63. Kjaergaard, H.G.; Garden, A.L.; Chaban, G.M.; Gerber, R.B.; Matthews, D.A.; Stanton, J.F. Calculation of vibrational transition frequencies and intensities in water dimer: Comparison of different vibrational approaches. *J. Phys. Chem. A* **2008**, *112*, 4324–4335. [[CrossRef](#)] [[PubMed](#)]
64. Kim, J.; Lee, J.Y.; Lee, S.; Mhin, B.J.; Kim, K.S. Harmonic vibrational frequencies of the water monomer and dimer: Comparison of various levels of ab initio theory. *J. Chem. Phys.* **1995**, *102*, 310–317. [[CrossRef](#)]
65. Yeo, G.A.; Ford, T.A. The combined use of ab initio molecular orbital theory and matrix isolation infrared spectroscopy in the study of molecular interactions. *Struct. Chem.* **1992**, *3*, 75–93. [[CrossRef](#)]
66. Liu, B.; McLean, A.D. Accurate calculation of the attractive interaction of two ground state helium atoms. *J. Chem. Phys.* **1973**, *59*, 4557–4558. [[CrossRef](#)]
67. Boys, S.F.; Bernardi, F. The calculation of small molecular interactions by the differences of separate total energies. Some procedures with reduced errors. *Mol. Phys.* **1970**, *19*, 553–566. [[CrossRef](#)]
68. Lane, J.R. CCSDTQ optimized geometry of water dimer. *J. Chem. Theory Comput.* **2013**, *9*, 316–323. [[CrossRef](#)]
69. Howard, J.C.; Gray, J.L.; Hardwick, A.J.; Nguyen, L.T.; Tschumper, G.S. Getting down to the fundamentals of hydrogen bonding: Anharmonic vibrational frequencies of (HF)₂ and (H₂O)₂ from Ab initio electronic structure computations. *J. Chem. Theory Comput.* **2014**, *10*, 5426–5435. [[CrossRef](#)]
70. Dunn, M.E.; Evans, T.M.; Kirschner, K.N.; Shields, G.C. Prediction of accurate anharmonic experimental vibrational frequencies for water clusters, (H₂O)_n, n = 2–5. *J. Phys. Chem. A* **2006**, *110*, 303–309. [[CrossRef](#)]
71. Feyereisen, M.W.; Feller, D.; Dixon, D.A. Hydrogen Bond Energy of the Water Dimer. *J. Phys. Chem.* **1996**, *100*, 2993–2997. [[CrossRef](#)]
72. Xu, X.; Goddard Iii, W.A. Bonding Properties of the Water Dimer: A Comparative Study of Density Functional Theories. *J. Phys. Chem. A* **2004**, *108*, 2305–2313. [[CrossRef](#)]
73. Dyke, T.R.; Muentzer, J.S. Microwave spectrum and structure of hydrogen bonded water dimer. *J. Chem. Phys.* **1974**, *60*, 2929–2930. [[CrossRef](#)]
74. Buczek, A.; Broda, M.A.; Kupka, T.; Kelterer, A.-M. Anharmonicity modeling in hydrogen bonded solvent dimers. *J. Mol. Liq.* **2021**, *339*, 116735. [[CrossRef](#)]
75. Řezáč, J. Non-Covalent Interactions Atlas benchmark data sets 5: London dispersion in an extended chemical space. *Phys. Chem. Chem. Phys.* **2022**, *24*, 14780–14793. [[CrossRef](#)] [[PubMed](#)]
76. Dyke, T.R.; Mack, K.M.; Muentzer, J.S. The structure of water dimer from molecular beam electric resonance spectroscopy. *J. Chem. Phys.* **1976**, *71*, 498–510. [[CrossRef](#)]
77. Wuelfert, S.; Herren, D.; Leutwyler, S. Supersonic jet CARS spectra of small water clusters. *J. Chem. Phys.* **1987**, *86*, 3751–3753. [[CrossRef](#)]
78. Amos, R.D. Structures, harmonic frequencies and infrared intensities of the dimers of H₂O and H₂S. *Chem. Phys.* **1986**, *104*, 145–151. [[CrossRef](#)]
79. Bentwood, R.M.; Barnes, A.J.; Orville-Thomas, W.J. Studies of intermolecular interactions by matrix isolation vibrational spectroscopy: Self-association of water. *J. Mol. Spectrosc.* **1980**, *84*, 391–404. [[CrossRef](#)]
80. Schofield, D.P.; Kjaergaard, H.G. Calculated OH-stretching and HOH-bending vibrational transitions in the water dimer. *Phys. Chem. Chem. Phys.* **2003**, *5*, 3100–3105. [[CrossRef](#)]
81. Scott, A.P.; Radom, L. Harmonic vibrational frequencies: An evaluation of Hartree-Fock, Moeller-Plesset, quadratic configuration interaction, density functional theory, and semiempirical scale factors. *J. Phys. Chem.* **1996**, *100*, 16502–16513. [[CrossRef](#)]
82. Karle, J.; Brockway, L.O. An Electron Diffraction Investigation of the Monomers and Dimers of Formic, Acetic and Trifluoroacetic Acids and the Dimer of Deuterium Acetate. *J. Am. Chem. Soc.* **1944**, *66*, 574–584. [[CrossRef](#)]
83. Derissen, J.L. A reinvestigation of the molecular structure of acetic acid monomer and dimer by gas electron diffraction. *J. Mol. Struct.* **1971**, *7*, 67–80. [[CrossRef](#)]
84. Jones, R.E.; Templeton, D.H. The Crystal Structure of Acetic Acid. *Acta Cryst.* **1958**, *11*, 484–487. [[CrossRef](#)]
85. Kwei, G.H.; Curl, R.F. Microwave Spectrum of O18 Formic Acid and Structure of Formic Acid. *J. Chem. Phys.* **1960**, *32*, 1592–1594. [[CrossRef](#)]
86. Miliordos, E.; Xantheas, S.S. On the validity of the basis set superposition error and complete basis set limit extrapolations for the binding energy of the formic acid dimer. *J. Chem. Phys.* **2015**, *142*, 094311. [[CrossRef](#)]

87. Nagy, P.I.; Smith, D.A.; Alagona, G.; Ghio, C. Ab initio studies of free and monohydrated carboxylic acids in the gas phase. *J. Phys. Chem.* **1994**, *98*, 486–493. [CrossRef]
88. Nagy, P.I. The syn–anti equilibrium for the COOH group reinvestigated. Theoretical conformation analysis for acetic acid in the gas phase and in solution. *Comput. Theor. Chem.* **2013**, *1022*, 59–69. [CrossRef]
89. Maçôas, E.M.S.; Lundell, J.; Pettersson, M.; Khriachtchev, L.; Fausto, R.; Räsänen, M. Vibrational spectroscopy of cis- and trans-formic acid in solid argon. *J. Mol. Spectrosc.* **2003**, *219*, 70–80. [CrossRef]
90. Herzberg, G. *Electronic Spectra and Electronic Structure of Polyatomic Molecules*; Van Nostrand: New York, NY, USA, 1966.
91. Käser, S.; Boittier, E.D.; Upadhyay, M.; Meuwly, M. Transfer Learning to CCSD(T): Accurate Anharmonic Frequencies from Machine Learning Models. *J. Chem. Theory Comput.* **2021**, *17*, 3687–3699. [CrossRef]
92. NIST. CCSD(T)/aQZ Harmonic Result. Available online: <https://cccbdb.nist.gov/energy3x.asp?method=63&basis=26&charge=0> (accessed on 22 January 2022).
93. Socha, O.; Dračinský, M. Dimerization of Acetic Acid in the Gas Phase—NMR Experiments and Quantum-Chemical Calculations. *Molecules* **2020**, *25*, 2150. [CrossRef]
94. Kollipost, F.; Larsen, R.W.; Domanskaya, A.V.; Nörenberg, M.; Suhm, M.A. Communication: The highest frequency hydrogen bond vibration and an experimental value for the dissociation energy of formic acid dimer. *J. Chem. Phys.* **2012**, *136*, 151101. [CrossRef] [PubMed]
95. Kalescky, R.; Kraka, E.; Cremer, D. Local vibrational modes of the formic acid dimer—The strength of the double hydrogen bond. *Mol. Phys.* **2013**, *111*, 1497–1510. [CrossRef]
96. Kalescky, R.; Kraka, E.; Cremer, D. Accurate determination of the binding energy of the formic acid dimer: The importance of geometry relaxation. *J. Chem. Phys.* **2014**, *140*, 084315. [CrossRef]
97. Bertie, J.E.; Michaelian, K.H. The Raman spectra of gaseous formic acid -h2 and -d2. *J. Chem. Phys.* **1982**, *76*, 886–894. [CrossRef]
98. Olbert-Majkut, A.; Ahokas, J.; Lundell, J.; Pettersson, M. Raman spectroscopy of formic acid and its dimers isolated in low temperature argon matrices. *Chem. Phys. Lett.* **2009**, *468*, 176–183. [CrossRef]
99. Tew, D.P.; Mizukami, W. Ab Initio Vibrational Spectroscopy of cis- and trans-Formic Acid from a Global Potential Energy Surface. *J. Phys. Chem. A* **2016**, *120*, 9815–9828. [CrossRef]
100. Barone, V.; Biczysko, M.; Bloino, J. Fully anharmonic IR and Raman spectra of medium-size molecular systems: Accuracy and interpretation. *Phys. Chem. Chem. Phys.* **2014**, *16*, 1759–1787. [CrossRef]
101. Farfán, P.; Echeverri, A.; Diaz, E.; Tapia, J.D.; Gómez, S.; Restrepo, A. Dimers of formic acid: Structures, stability, and double proton transfer. *J. Chem. Phys.* **2017**, *147*, 044312. [CrossRef]
102. Marushkevich, K.; Khriachtchev, L.; Lundell, J.; Domanskaya, A.; Räsänen, M. Matrix Isolation and Ab Initio Study of Trans–Trans and Trans–Cis Dimers of Formic Acid. *J. Phys. Chem. A* **2010**, *114*, 3495–3502. [CrossRef]
103. Kelemen, A.K.; Lubert, S. On the vibrations of formic acid predicted from first principles. *Phys. Chem. Chem. Phys.* **2022**, *24*, 28109–28120. [CrossRef]
104. Krishnakumar, P.; Maity, D.K. Theoretical studies on dimerization vs. microhydration of carboxylic acids. *Comput. Theor. Chem.* **2017**, *1099*, 185–194. [CrossRef]
105. Almennigen, A.; Bastiansen, O.; Motzfeldt, T. A reinvestigation of the structure of monomer and dimer formic acid by gas electron diffraction technique. *Acta Chem. Scand.* **1969**, *23*, 2848–2864. [CrossRef]
106. Gora, R.W.; Grabowski, S.J.; Leszczynski, J. Dimers of Formic Acid, Acetic Acid, Formamide and Pyrrole-2-carboxylic Acid: an Ab Initio Study. *J. Phys. Chem. A* **2005**, *109*, 6397–6405. [CrossRef] [PubMed]
107. Burns, L.A.; Marshall, M.S.; Sherrill, C.D. Comparing Counterpoise-Corrected, Uncorrected, and Averaged Binding Energies for Benchmarking Noncovalent Interactions. *J. Chem. Theory Comput.* **2014**, *10*, 49–57. [CrossRef]
108. Okrański, P.; Latajka, Z.; Hättig, C. Theoretical Study on Noncovalent Interactions in the Carbon Nanotube–Formic Acid Dimer System. *J. Phys. Chem. C* **2014**, *118*, 4483–4488. [CrossRef]
109. NIST. *Computational Chemistry Comparison and Benchmark DataBase Release 22 (May 2022) Standard Reference Database 101*; NIST: Gaithersburg, MD, USA, 2022.
110. Maréchal, Y. IR spectra of carboxylic acids in the gas phase: A quantitative reinvestigation. *J. Chem. Phys.* **1987**, *87*, 6344–6353. [CrossRef]
111. Takatani, T.; Hohenstein, E.G.; Malagoli, M.; Marshall, M.S.; Sherrill, C.D. Basis set consistent revision of the S22 test set of noncovalent interaction energies. *J. Chem. Phys.* **2010**, *132*, 144104. [CrossRef]
112. Marshall, M.S.; Burns, L.A.; Sherrill, C.D. Basis set convergence of the coupled-cluster correction, δ MP2CCSD(T): Best practices for benchmarking non-covalent interactions and the attendant revision of the S22, NBC10, HBC6, and HSG databases. *J. Chem. Phys.* **2011**, *135*, 194102. [CrossRef]
113. Marshall, M.S.; Sherrill, C.D. Dispersion-Weighted Explicitly Correlated Coupled-Cluster Theory [DW-CCSD(T**)-F12]. *J. Chem. Theory Comput.* **2011**, *7*, 3978–3982. [CrossRef]
114. Dudev, M.; Wang, J.; Dudev, T.; Lim, C. Factors Governing the Metal Coordination Number in Metal Complexes from Cambridge Structural Database Analyses. *J. Phys. Chem. B* **2006**, *110*, 1889–1895. [CrossRef]
115. Wang, X.; Andrews, L. Infrared Spectra and Electronic Structure Calculations for the Group 2 Metal M(OH)₂ Dihydroxide Molecules. *J. Phys. Chem. A* **2005**, *109*, 2782–2792. [CrossRef] [PubMed]

116. Sullivan, M.B.; Iron, M.A.; Redfern, P.C.; Martin, J.M.L.; Curtiss, L.A.; Radom, L. Heats of Formation of Alkali Metal and Alkaline Earth Metal Oxides and Hydroxides: Surprisingly Demanding Targets for High-Level ab Initio Procedures. *J. Phys. Chem. A* **2003**, *107*, 5617–5630. [CrossRef]
117. Makieieva, N.; Kupka, T.; Stobiński, L.; Małolepszy, A. Modeling hydration of graphene oxide (GO)—Does size matter? *J. Mol. Struct.* **2024**, *1318*, 139317. [CrossRef]
118. Van Gaalen, K.E.; Flanagan, L.B.; Peddle, D.R. Photosynthesis, chlorophyll fluorescence and spectral reflectance in Sphagnum moss at varying water contents. *Oecologia* **2007**, *153*, 19–28. [CrossRef]
119. Hyyryläinen, A.; Rautio, P.; Turunen, M.; Huttunen, S. Seasonal and inter-annual variation in the chlorophyll content of three co-existing Sphagnum species exceeds the effect of solar UV reduction in a subarctic peatland. *SpringerPlus* **2015**, *4*, 478. [CrossRef]
120. Proctor, M.C.F. Climatic Responses and Limits of Bryophytes: Comparisons and Contrasts with Vascular Plants. In *Bryophyte Ecology and Climate Change*; Tuba, Z., Slack, N.G., Stark, L.R., Eds.; Cambridge University Press: Cambridge, UK, 2011; pp. 35–54.
121. Nagase, A.; Katagiri, T.; Lundholm, J. Investigation of moss species selection and substrate for extensive green roofs. *Ecol. Eng.* **2023**, *189*, 106899. [CrossRef]
122. Demková, L.; Baranová, B.; Oboňa, J.; Árvay, J.; Lošák, T. Assessment of air pollution by toxic elements on petrol stations using moss and lichen bag technique. *Plant Soil Environ.* **2017**, *63*, 355–361. [CrossRef]
123. Lichtenthaler, H.K.; Buschmann, C.; Knapp, M. How to correctly determine the different chlorophyll fluorescence parameters and the chlorophyll fluorescence decrease ratio RfD of leaves with the PAM fluorometer. *Photosynthetica* **2005**, *43*, 379–393. [CrossRef]
124. ICP Vegetation. Heavy Metals, Nitrogen and Pops in European Mosses: 2020 Survey. Available online: <https://icpvegetation.ceh.ac.uk/sites/default/files/ICP%20Vegetation%20moss%20monitoring%20manual%202020.pdf> (accessed on 27 May 2024).
125. Jóźwiak, M.A.; Rybiński, P. Assessment of air pollution along express roads and motorways of varied traffic load with the use of bioindicators. *Rocz.Świętokrzyski Seria B Nauki Przyr. Kieleckie Tow. Nauk.* **2013**, *34*, 51–63. Available online: https://rocznikswietokrzyski.pl/wp-content/uploads/2015/01/Jozwiak_Rybinski.pdf (accessed on 27 May 2024).
126. Frisch, M.J.; Trucks, G.W.; Schlegel, H.B.; Scuseria, G.E.; Robb, M.A.; Cheeseman, J.R.; Scalmani, G.; Barone, V.; Petersson, G.A.; Nakatsuji, H.; et al. *Gaussian 16 Rev. C.01*; Gaussian: Wallingford, CT, USA, 2016.
127. Lee, C.; Yang, W.; Parr, R.G. Development of the Colle-Salvetti Correlation-Energy Formula into a Functional of the Electron Density. *Phys. Rev. B* **1988**, *37*, 785–789. [CrossRef]
128. Vosko, S.H.; Wilk, L.; Nusair, M. Accurate spin-dependent electron liquid correlation energies for local spin density calculations: A critical analysis. *Can. J. Phys.* **1980**, *58*, 1200–1211. [CrossRef]
129. Stephens, P.J.; Devlin, F.J.; Chabalowski, C.F.; Frisch, M.J. Ab Initio Calculation of Vibrational Absorption and Circular Dichroism Spectra Using Density Functional Force Fields. *J. Phys. Chem.* **1994**, *98*, 11623–11627. [CrossRef]
130. Becke, A.D. Density-functional exchange-energy approximation with correct asymptotic behavior. *Phys. Rev. A* **1988**, *38*, 3098–3100.
131. Kupka, T.; Buczek, A.; Broda, M.A.; Stachow, M.; Tarnowski, P. DFT studies on the structural and vibrational properties of polyenes. *J. Mol. Model.* **2016**, *22*, 101. [CrossRef] [PubMed]
132. Kupka, T.; Buczek, A.; Broda, M.A.; Szostak, R.; Lin, H.M.; Fan, L.W.; Wrzalik, R.; Stobinski, L. Modeling red coral (*Corallium rubrum*) and African snail (*Helix aspersa*) shell pigments: Raman spectroscopy versus DFT studies. *J. Raman Spectrosc.* **2016**, *47*, 908–916. [CrossRef]
133. Dunning, T.H., Jr. Gaussian basis sets for use in correlated molecular calculations. I. The atoms boron through neon and hydrogen. *J. Chem. Phys.* **1989**, *90*, 1007–1023. [CrossRef]
134. Kendall, R.A.; Dunning, T.H., Jr.; Harrison, R.J. Electron affinities of the first-row atoms revisited. Systematic basis sets and wave functions. *J. Chem. Phys.* **1992**, *96*, 6796–6806. [CrossRef]
135. Woon, D.E.; Dunning, T.H., Jr. Gaussian basis sets for use in correlated molecular calculations. III. The atoms aluminum through argon. *J. Chem. Phys.* **1993**, *98*, 1358–1371. [CrossRef]
136. Woon, D.E.; Dunning, T.H., Jr. Benchmark calculations with correlated molecular wave functions. I. Multireference configuration interaction calculations for the second row diatomic hydrides. *J. Chem. Phys.* **1993**, *99*, 1914.
137. Grimme, S.; Antony, J.; Ehrlich, S.; Krieg, S. A consistent and accurate ab initio parametrization of density functional dispersion correction (dft-d) for the 94 elements H-Pu. *J. Chem. Phys.* **2010**, *132*, 154104. [CrossRef]
138. Grimme, S.; Ehrlich, S.; Goerigk, L. Effect of the damping function in dispersion corrected density functional theory. *J. Comput. Chem.* **2011**, *32*, 1456–1465. [CrossRef] [PubMed]
139. Dziurawicz, P.; Fałowska, P.; Waszkiewicz, K.; Wietrzyk-Pełka, P.; Węgrzyn, M. Effect of light stress on maximum photochemical efficiency of photosystem II and chloroplast structure in cryptogams *Cladonia mitis* and *Pleurozium schreberi*. *Ecol. Quest.* **2024**, *35*, 1–29. [CrossRef]
140. Loriaux, S.D.; Avenson, T.J.; Welles, J.M.; Mcdermitt, D.K.; Eckles, R.D.; Riensche, B.; Genty, B. Closing in on maximum yield of chlorophyll fluorescence using a single multiphase flash of sub-saturating intensity. *Plant. Cell. Environ.* **2013**, *36*, 1755–1770. [CrossRef] [PubMed]
141. Šraj Kržič, N.; Gaberščik, A. Photochemical efficiency of amphibious plants in an intermittent lake. *Aquat. Bot.* **2005**, *83*, 281–288. [CrossRef]
142. Nekhoroshkov, P.; Peshkova, A.; Zinicovscaia, I.; Vergel, K.; Kravtsova, A. Assessment of the Atmospheric Deposition of Heavy Metals and Other Elements in the Mountain Crimea Using Moss Biomonitoring Technique. *Atmosphere* **2022**, *13*, 573. [CrossRef]

143. Chaligava, O.; Shetekauri, S.; Badawy, W.M.; Frontasyeva, M.V.; Zinicovscaia, I.; Shetekauri, T.; Kvlividze, A.; Vergel, K.; Yushin, N. Characterization of Trace Elements in Atmospheric Deposition Studied by Moss Biomonitoring in Georgia. *Arch. Environ. Contam. Toxicol.* **2021**, *80*, 350–367. [[CrossRef](#)]
144. Olbert-Majkut, A.; Ahokas, J.; Lundell, J.; Pettersson, M. Raman spectroscopy of acetic acid monomer and dimers isolated in solid argon. *J. Raman Spectrosc.* **2011**, *42*, 1670–1681. [[CrossRef](#)]
145. Qu, C.; Bowman, J.M. High-dimensional fitting of sparse datasets of CCSD(T) electronic energies and MP2 dipole moments, illustrated for the formic acid dimer and its complex IR spectrum. *J. Chem. Phys.* **2018**, *148*, 241713. [[CrossRef](#)]

Disclaimer/Publisher’s Note: The statements, opinions and data contained in all publications are solely those of the individual author(s) and contributor(s) and not of MDPI and/or the editor(s). MDPI and/or the editor(s) disclaim responsibility for any injury to people or property resulting from any ideas, methods, instructions or products referred to in the content.